

THE NATURE OF LINER-LIKE EMISSION IN RED GALAXIES

RENBIN YAN¹, MICHAEL R. BLANTON¹

¹ Center for Cosmology and Particle Physics, Department of Physics, New York University, New York, NY, 10003; ry9@nyu.edu
Draft version February 18, 2022

ABSTRACT

Passive red galaxies frequently contain warm ionized gas and have spectra similar to low-ionization nuclear emission-line regions (LINERs). Here we investigate the nature of the ionizing sources powering this emission, by comparing nuclear spectroscopy from the Palomar survey with larger aperture data from the Sloan Digital Sky Survey. We find the line emission in the majority of passive red galaxies is spatially extended; the H α surface brightness profile depends on radius r as $r^{-1.28}$. We detect strong line ratio gradients with radius in [N II]/H α , [S II]/H α , and [O III]/[S II], requiring the ionization parameter to increase outwards. Combined with a realistic gas density profile, this outward increasing ionization parameter convincingly rules out AGN as the dominant ionizing source, and strongly favors distributed ionizing sources. Sources that follow the stellar density profile can additionally reproduce the observed luminosity-dependence of the line ratio gradient. Post-AGB stars provide a natural ionization source candidate, though they have an ionization parameter deficit. Velocity width differences among different emission lines disfavor shocks as the dominant ionization mechanism, and suggest that the interstellar medium in these galaxies contains multiple components. We conclude that the line emission in most LINER-like galaxies found in large aperture (> 100 pc) spectroscopy is not primarily powered by AGN activity and thus does not trace the AGN bolometric luminosity. However, they can be used to trace warm gas in these red galaxies.

Subject headings: galaxies:active — galaxies: ISM — galaxies: elliptical and lenticular — galaxies: emission lines — ISM: kinematics and dynamics — stars: AGB and post-AGB

1. INTRODUCTION

Emission lines are important spectral features that can help us probe the gaseous component in galaxies. They are not unique to star-forming galaxies, but also exist in galaxies with only old stellar populations. Numerous results (Phillips et al. 1986; Goudfrooij et al. 1994; Yan et al. 2006) have shown that line emission is prevalent in more than 50% of passive red galaxies, and they have line ratios similar to the low ionization nuclear emission line regions (LINERs, Heckman 1980). What powers this line emission has been an unsettled question for decades.

LINERs are identified by their particular pattern of line strength ratios, with strong low-ionization forbidden lines (e.g. [N II], [S II], [O II], [O I]) relative to recombination lines (e.g. H α , H β) and high-ionization forbidden lines (e.g. [O III]). Unlike galaxies dominated by star-forming HII regions or Seyferts, whose line ratio patterns clearly identify their ionizing sources as young massive stars or active galactic nuclei (AGN), respectively, LINERs can be produced by a wide array of ionization mechanisms, such as photo-ionization by an AGN (Ferland & Netzer 1983; Halpern & Steiner 1983; Groves et al. 2004b), photoionization by post-AGB stars (Binette et al. 1994), fast radiative shocks (Dopita & Sutherland 1995), photoionization by the hot X-ray-emitting gas (Voit & Donahue 1990; Donahue & Voit 1991), or thermal conduction from the hot gas (Sparks et al. 1989). Therefore, their exact ionization mechanism has been hotly debated.

The LINER puzzle is further complicated by the limited spatial resolution available in many samples, par-

ticularly in SDSS. Originally, “LINER” only referred to a class of galaxy nuclei. They were first identified in *nuclear* spectra of nearby galaxies (Heckman 1980). This is the case in most LINER studies of nearby galaxies (e.g. Ho et al. 1997b). For our discussion, we refer to these LINERs as “nuclear LINERs.” We should keep in mind that ground-based slit spectra, under typical seeing, usually cannot resolve better than the central few hundred parsecs for even nearby galaxies ($\lesssim 40$ Mpc). This is the scale referred to by the word ‘nuclear’. With narrow band imaging and/or long-slit spectroscopy surveys, Phillips et al. (1986), Kim (1989), Buson et al. (1993), Goudfrooij et al. (1994), Macchetto et al. (1996), Zeilinger et al. (1996), and others found that the line emission in early-type galaxies is often extended to kpc scale and has LINER-like line ratios. We refer to these cases as “extended LINERs.” In surveys of much more distant galaxies, such as most galaxies in SDSS, or surveys at high redshifts, such as DEEP2 (Davis et al. 2003), zCOSMOS (Lilly et al. 2007), BOSS (Eisenstein et al. 2011), and distant cluster surveys (e.g. Lubin et al. 2009), the spectra obtained usually covers a much larger scale than the nuclei and we are not always able to tell how the emission is distributed spatially. Still, a large number of galaxies show LINER-like spectra (Yan et al. 2006; Lemaux et al. 2010; Bongiorno et al. 2010; Yan et al. 2011). The term “LINER” is often casually adopted in this case to refer to galaxies with LINER-like spectra. Here, we refer to these cases as “LINER-like galaxies.”

Although the name of LINER includes a morphological description — “nuclear”, there has been no quantitative definition of what line emission distribution would qual-

ify as a nuclear LINER. All LINERs have been defined only spectroscopically based on their line ratio pattern. The distinction between nuclear LINERs and extended LINERs is very murky. Practically, it often refers to the scale over which the spectrum is taken — $\lesssim 200$ pc for nuclear and $\gtrsim 1$ kpc for extended, rather than a characteristic scale or morphological description of the line emission distribution. Masegosa et al. (2011) tried to classify the different morphologies of nuclear line emission distribution based on narrow band HST images. In the large majority of LINERs (84%), they found an unresolved nuclear source surrounded by diffuse emission extending to a few hundreds of parsecs. However, it is unclear in those data whether the two components have different ionizing sources and which component dominates in total luminosity.

For a large fraction of nuclear LINERs, which are defined using spectra from the central few hundred parsecs, AGN activity clearly exists in the center, although some puzzles still remain. Evidence for AGN activity includes the detection of central hard X-ray point sources, compact radio cores, broad emission lines in direct or polarized light, and UV variability (see Ho 2008 and references therein). On the other hand, there is growing evidence (Ho et al. 2001; Eracleous et al. 2010) that the weak AGN in most nuclear LINERs does not emit enough photoionizing photons to account for the observed intensity in optical emission lines. Based on narrowband images or slit spatial profiles observed from HST, the narrow line region in LINERs appear to be strongly concentrated in the center, with typical dimensions smaller than tens of parsecs (Walsh et al. 2008). However, in some objects the profile can extend to a few hundred parsecs (Shields et al. 2007). Thus, even for nuclear LINERs, whether the AGN is responsible for all of the narrow line emission within the central few hundred parsecs is unclear.

For the extended LINERs, it is totally unclear how they are related with nuclear LINERs and what mechanism powers their line emission. For LINER-like galaxies, we know even less. Are they very powerful nuclear LINERs or are they dominated by extended LINER emission? The nuclear-LINER fraction among early-type galaxies is fairly similar to the LINER-like galaxy fraction among red galaxies in SDSS (Ho et al. 1997b; Yan et al. 2006). Is this similarity fortuitous, or is there a physical connection? We try to answer these questions in this paper.

Solving these puzzles is important. Many people have used the line strength in LINER-like galaxies from SDSS as an indicator of AGN power (Kauffmann et al. 2003; Constantin & Vogeley 2006; Kewley et al. 2006; Schawinski et al. 2007; Kauffmann & Heckman 2009), while others argued they are not genuine AGNs (Stasińska et al. 2008; Sarzi et al. 2010; Cid Fernandes et al. 2011; Capetti & Baldi 2011) but more likely powered by hot evolved stars. Therefore, settling this puzzle is not only important for AGN demographics, but also for understanding the ISM in early-type galaxies. If the line strength is not an AGN indicator, it might instead reflect the amount of cool gas supply, or the cooling rate of the hot gas. To make the correct physical connections, we have to first find out what powers the line emission. Additionally, if we can

pin down the ionization mechanism, we will be able to measure the gas-phase metallicity in these red galaxies, which has so far been impossible.

For the extended LINER emission, three types of evidence have been presented to argue that they are not powered by AGN. (a) Post-AGBs could produce enough photo-ionizing photons (di Serego Alighieri et al. 1990; Binette et al. 1994; Stasińska et al. 2008). (b) The line emission regions are spatially extended with a surface brightness profile that is shallower than r^{-2} (Sarzi et al. 2010). (c) The line luminosity correlates with stellar luminosity (Sarzi et al. 2010; Capetti & Baldi 2011). This evidence led to the reasonable suspicion that a population of hot evolved stars might in fact dominate over the AGN photoionization in early-type galaxies. However, all of these arguments depends on inherent assumptions about observationally unknown factors.

For the first argument, di Serego Alighieri et al. (1990), Binette et al. (1994), and Stasińska et al. (2008) all assumed that nearly all the photons produced by post-AGB stars are absorbed by the gas and that the gas is distributed near the ionizing stars to produce the correct ionization parameter. Both the gas covering factor and the relative distribution of gas to stars are unknown.

For the second argument, Sarzi et al. (2006, 2010) showed that the line emission in nearly all line-emitting early-type galaxies is spatially extended, and has a surface brightness profile shallower than r^{-2} . Although Sarzi et al. (2010) is very careful in not drawing conclusions based on this fact alone, such extended emission has been quoted by many others (e.g. Kaviraj 2010; Masters et al. 2010; Schawinski et al. 2010) as evidence for stellar photoionization. However, a central point source can also produce extended line emission regions. The line emission surface brightness profile not only depends on the ionizing flux profile, but also depends on how the gas filling factor, spatial distribution of gas clouds, and the gas density vary with radius. Both the filling factor and the cloud spatial distribution are so poorly known that the surface brightness profile provides no practical constraint on the flux profile.

The third argument is based on the observed correlation in surface brightness between line emission and stellar continuum. Sarzi et al. (2010) showed with IFU data that the $H\beta$ equivalent width (EW) is fairly constant throughout each galaxy when excluding the nuclear region; Capetti & Baldi (2011) argued a similar point based on integrated line emission from SDSS. This might seem like the strongest support for stellar photoionization. However, as mentioned above, the line flux depends on many other unconstrained factors besides the ionizing flux, such as the gas filling factor. Sarzi et al. (2010) performed the calculation for a simple model of stellar photoionization and found that it did not produce the spatially-invariant EW of $H\beta$ they found throughout each galaxy in their sample. To make the model consistent with observations, certain fine tuning of the gas filling factor, density, and/or mean-free path of the ionizing photons is required, which has no independent observational support.

In fact, as long as both the line flux and stellar continuum are strong functions with radius in these galaxies, one would always find tight correlation between the two, even in the case of photoionization by an AGN.

Thus, we need a simpler test that can distinguish different ionization mechanisms that is free of assumptions about unknown parameters. A central point source (e.g. AGN) and a system of spatially distributed ionizing sources will produce different ionizing flux profiles as a function of radius. Thus, for the same gas density profile, they would yield different ionization parameter profiles, leading to different spatial gradients in line ratios. Thus, looking at the line ratio gradients may provide a clue to differentiate the two scenarios. The only assumption involved here is the gas density profile, which can be derived from the hot gas density profile assuming pressure equilibrium or can be measured directly from line ratios.

Ideally, the line ratio gradient is best measured from integral field spectroscopy (IFS) data. However, current IFS data (SAURON, Bacon et al. 2001; ATLAS3D, Cappellari et al. 2011) have very limited wavelength coverage and do not probe enough strong emission lines to detect the ionization gradient in a large number of galaxies. The emission lines covered by SAURON are [O III], H β , and in a few cases [N I] λ 5197,5200. Because [O III]/H β depends on the ionization parameter and to some extent also on the hardness of the ionizing spectra, it alone does not provide an unambiguous constraint on the ionization gradient. In addition, the weakness of H β makes it more difficult to detect small changes.

Our solution is to use the nuclear spectra from the Palomar survey (Ho et al. 1995), and the fiber spectra from SDSS. By identifying the same population of galaxies at different redshifts, for which the fixed angular aperture corresponds to different physical radii, we can study statistically the spatial profile of emission line surface brightness and the line ratio gradient. The emission line surface brightness profile can also inform us about the relationship between nuclear LINERs and extended LINERs.

In addition, we will examine the widths of emission lines. Different forbidden lines will have different widths if there is line ratio variation within a galaxy and the variation is correlated with gas kinematics. On the other hand, shock ionization models also should produce width differences among multiple lines due to the dependence of line ratios on shock velocity.

Our investigation includes all line-emitting red galaxies except for those containing star formation; we do not specifically select for LINER-like galaxies. Based on line ratio diagnostics, these line-emitting red galaxies do have fairly uniform line ratios with the most typical case belonging to the LINER category, as shown by the line ratio diagnostic diagram in Figure 1. Avoiding the use of line ratios in sample selection is essential for our study of the line ratio gradient.

This paper is organized as following. In Section 2, we will describe the data, measurements, and sample selection. In Section 3, we will investigate the relationship between nuclear LINERs and extended LINERs and derive an average emission line surface brightness profile. In Section 4, we will show the line ratio gradient. In Section 5, we will present the line width differences. In Section 6, we discuss the viability of each ionization mechanism in explaining the line ratio gradient and line width differences. We conclude in Section 7.

Throughout this paper, we use a flat Λ CDM cosmology with $\Omega_m = 0.3$, and a Hubble constant of $H_0 =$

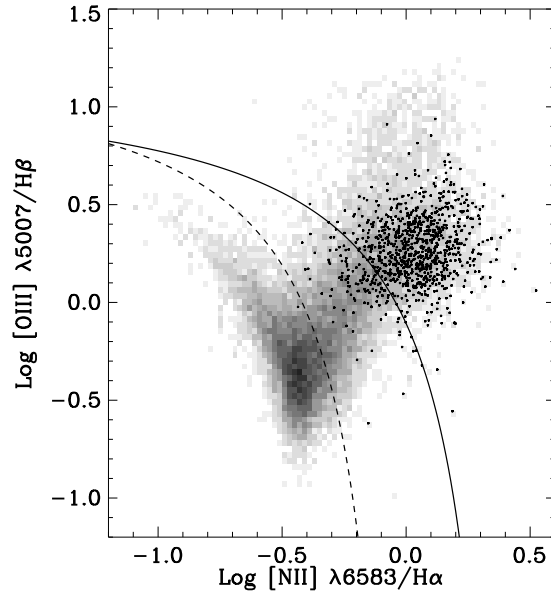


FIG. 1.— Line ratio diagnostic diagram for SDSS galaxies (gray scale) at $0.09 < z < 0.1$ with all four emission lines detected at more than 3σ significance, and the passive red galaxies (black points) among them. The latter is selected according to the criteria described in Section 2.4. The curves represent demarcations defined by Kewley et al. (2001) (solid) and Kauffmann et al. (2003) (dashed). This illustrates that red galaxies have fairly uniform line ratios which puts most of them in the LINER-like galaxy category.

$75h_{75}\text{kms}^{-1}\text{Mpc}^{-1}$ with $h_{75} = 1$. This Hubble constant is chosen to make the comparison easier with the data presented by Ho et al. (1997a). All the magnitude used are in the AB system.

2. DATA AND MEASUREMENTS

To investigate the luminosity and line ratio gradient, we compare line luminosity and line ratio measurements between different physical apertures for the same population of galaxies. The Palomar survey (Ho et al. 1995) provides us the best sample for nuclear aperture measurements. The SDSS survey can provide consecutively larger aperture measurements if we select identical samples at consecutively higher redshifts.

2.1. Data

In the Palomar survey, nuclear spectrum were taken for a sample of ~ 500 local galaxies, selected from the Revised Shapley-Ames Catalog of Bright Galaxies (RSA; Sandage & Tammann 1981) and the Second Reference Catalogue of Bright Galaxies (RC2; de Vaucouleurs et al. 1976) with the criteria of $B_T < 12.5$ (Vega magnitudes) and $\delta > 0$. The nuclear regions (~ 200 pc) of these galaxies are isolated using a $2'' \times 4''$ aperture. The details of data reduction, stellar continuum subtraction, and line measurements can be found in Ho et al. (1995).

We also employ data from the Sloan Digital Sky Survey (York et al. 2000; Stoughton et al. 2002) Data Release Seven (Abazajian et al. 2009). Using two fiber-fed spectrographs on a dedicated 2.5-m telescope, SDSS has obtained high quality spectra for roughly half a million

galaxies with $r < 17.77$ in the wavelength range of 3800–9200Å with a resolution of $R \sim 2000$. The SDSS fibers have a fixed aperture of 3" diameter, which corresponds to different physical scales at different distances.

The SDSS spectroscopic data used here have been reduced through the Princeton spectroscopic reduction pipeline, which produces the flux- and wavelength-calibrated spectra.¹ The redshift catalog of galaxies used is from the NYU Value Added Galaxy Catalog (DR7)² (Blanton et al. 2005). K-corrections for SDSS were derived using Blanton & Roweis (2007)'s *kcorrect* package (v4.2).

2.2. Emission line measurements

For emission line measurements in the Palomar sample, we adopt the tabulated values provided by Ho et al. (1997a).

For the SDSS sample, we measured the emission lines in the spectra after a careful subtraction of the stellar continua. The code used is an updated version of the code used by Yan et al. (2006). The major updates are:

1. We apply an additional flux calibration to all of SDSS spectra to fix small scale calibration residuals (Yan 2011). This is critically important for our results. We describe this correction in more detail below.
2. The absolute flux is calibrated for each spectrum by matching the synthetic r -band magnitude with the r -band fiber magnitude. The spectra are also corrected for Galactic extinction.
3. The stellar continuum is modelled as a non-negative linear combination of 7 templates. The templates are seven simple stellar population models with solar metallicity, with ages of 0.125, 0.25, 0.5, 1, 2, 7, and 13 Gyrs, made using the Bruzual & Charlot (2003) stellar population models.

As in Yan et al. (2006), the emission line flux is measured from direct flux-summing in the continuum-subtracted spectra. The line windows and sidebands are unchanged.

We discovered that the flux calibration produced by the standard SDSS pipeline has percent-level small-scale residuals that can significantly impact the measurement of emission line flux when the equivalent width of the line is low (a few Angstroms; see Yan 2011 Fig. 1 for an example of the impact). For example, for an emission line EW of 1Å measured in a 20Å window, if the throughput differs by 1% between the central window and the sidebands where the continuum level is measured, the line flux measurement will be off by 20%. This will introduce systematic offsets in line flux and line ratios as a function of redshift, significantly hampering our investigation. Therefore, we need a much more accurate small scale flux calibration than what the standard pipeline produces.

Yan (2011) solved this problem by comparing stacked red-sequence spectra between small redshift intervals to

statistically determine the relative throughput as a function of wavelength, and achieved an flux calibration accuracy of 0.1% on scales of a few hundred Angstrom. We applied this small scale flux calibration to the spectra. This calibration is essential for the result presented in this paper (see Fig. 6 in Yan 2011).

In this paper, we also make use of the line width measurements for the SDSS sample. The line widths are measured by fitting Gaussians to each emission line. Different emission lines are allowed to have different widths, except that the two [S II] lines (6716Å and 6731Å) and the two [N II] lines (6548Å and 6584Å) are both forced to have the same width. The instrumental resolution of SDSS varies with wavelength, the position of the fiber on the focal plane, and the spectrograph. This varying resolution as a function of wavelength is given for each individual spectrum by the Princeton pipeline. We subtracted quadratically the instrumental broadening from the measured line width to derive the intrinsic width of each emission line for each galaxy. Our quoted uncertainty of the line width measurement is the formal uncertainty of the Gaussian fit.

2.3. Photometry

To identify the same population of galaxies at different redshifts, we use a photometric selection. We intentionally avoid the use of line ratios in sample selection to avoid bias on the line ratio gradient estimates.

For the Palomar survey, we took the catalog provided by Ho et al. (1997a). Photometric information is available from the Third Reference Catalogue of Bright Galaxies (RC3; de Vaucouleurs et al. 1991) but is incomplete. To increase the sample size with available photometry and to put them on the same system as the SDSS galaxies, we re-measured photometry for those galaxies inside the SDSS footprint using the SDSS images. We employed an improved background subtraction technique (Blanton et al. 2011) to treat these nearby large galaxies properly. After proper background subtraction, mosaicking, and deblending, we measure the photometry by fitting a two-dimensional Sersic profile to the deblended galaxy image. In the end, we derive the Galactic extinction corrected restframe B and V magnitudes for these galaxies from the measured g and r magnitudes using the *kcorrect* software package (v4.2, Blanton & Roweis 2007).

For those galaxies outside the SDSS footprint and for certain Messier objects for which the new method does not yield satisfactory results, we take the photometric information from the RC3 catalog and convert them to the AB system, and then correct for Galactic extinction. We do not attempt to correct for internal extinction for these galaxies as such measurements are not available for the SDSS sample.

For the higher redshift SDSS spectroscopic sample we derived the B and V magnitudes from the SDSS magnitudes using the *kcorrect* package mentioned above.

2.4. Sample definition

Figure 2 shows the color-magnitude distribution for the Palomar sample overlaid on a sample of SDSS galaxies between $0.09 < z < 0.1$. The two samples have consistent color-magnitude distributions. We select only the red-

¹ <http://spectro.princeton.edu/>

² <http://sdss.physics.nyu.edu/vagc/>

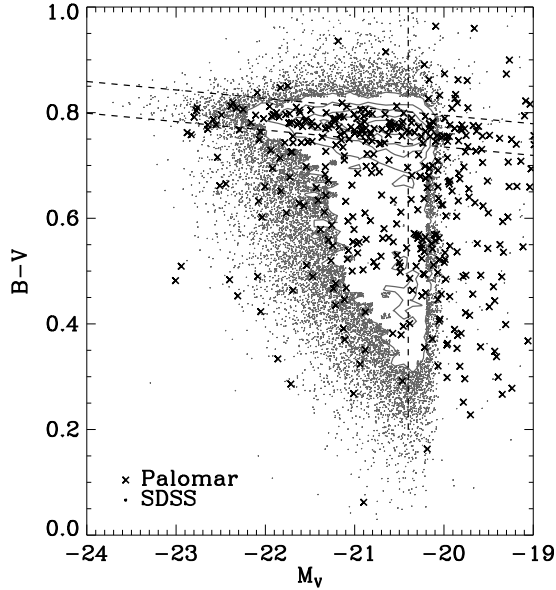


FIG. 2.— Color-magnitude distribution of the Palomar sample (dark crosses) and galaxies in SDSS with $0.09 < z < 0.1$ (contour and gray points). The lines indicate our color and magnitude cuts.

sequence galaxies in both samples using two stringent color cuts defined by

$$(B - V) > -0.016(M_V - 5 \log h_{75}) + 0.415 \quad (1)$$

$$(B - V) < -0.016(M_V - 5 \log h_{75}) + 0.475 \quad (2)$$

These cuts are chosen to reduce contamination from dusty star-forming galaxies. We limit to galaxies brighter than -20.4 in $M_V - 5 \log h_{75}$ to match the magnitude limit of the SDSS survey at $z \sim 0.10$.

There are 86 red galaxies in the Palomar survey satisfying these two cuts. Based on the morphological type given by the RC3 catalog, there are 30 ellipticals, 30 lenticulars, 15 early spirals (S0/a, Sa, Sab), 9 late spirals (Sb, Sbc, Sc) and 2 irregular galaxies. With the classification scheme given in Ho et al. (1997a), there are 29 LINER nuclei, 19 transition objects, 11 Seyferts and 3 HII regions. The remaining 24 objects have no line emission detectable in their nuclei.

In SDSS, we select a comparison sample with $0.01 < z < 0.1$ using the same color and absolute magnitude cuts. In most of our analysis, we bin the SDSS sample into 9 redshift bins with $\Delta z = 0.01$.

Despite our selection on color, red galaxies can have sufficient star formation to contribute to the line emission in our apertures, especially for the more distant galaxies. The morphological distribution of the Palomar red galaxy sample suggests that this is occurring, given the presence of late-type spirals. We would like to exclude star-forming spectra in our analysis, since we want to understand the origin of line emission not associated with star formation. Therefore, in the Palomar sample, we exclude galaxies with Hubble types later than S0 and those spectroscopically classified as HII nuclei. This removes 31% of the Palomar red sample. The remaining sample includes 19 LINERs, 13 transition objects, 6 Seyferts,

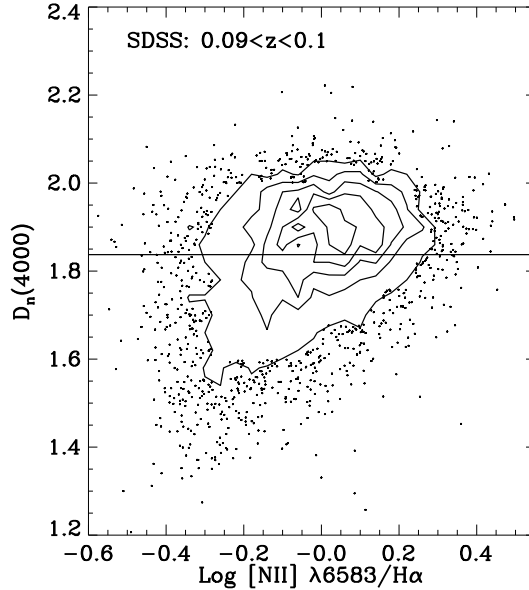


FIG. 3.— $D_n(4000)$ vs. $\log [\text{N II}]/\text{H}\alpha$ for red sequence galaxies in SDSS with $0.09 < z < 0.1$ and $M_V < -20.4$. We show only the brightest 50% of the sample in $\text{H}\alpha$ luminosity. We show our chosen threshold as the solid horizontal line; it is set at the 30-th percentile in the $D_n(4000)$ distribution of the whole sample. Those galaxies with low $D_n(4000)$ and low $[\text{N II}]/\text{H}\alpha$ probably have significant contribution by young massive stars in the production of their line emission.

and 21 quiescent galaxies.

To achieve a similar selection in the SDSS sample, we exclude galaxies with any star formation using a stringent cut on $D_n(4000)$ (Balogh et al. 1999). This quantity is a proxy for the light weighted mean stellar age, and is thus sensitive to small levels of star formation. Measured over two 100\AA windows separated by 50\AA , it is less affected by dust reddening than rest frame colors, and more robustly measured than the $\text{H}\delta_A$ equivalent width. Figure 3 shows the $D_n(4000)$ vs. $\log [\text{N II}]/\text{H}\alpha$ for those galaxies in the SDSS sample with $0.09 < z < 0.1$. Galaxies that have small $D_n(4000)$ also tend to have lower $[\text{N II}]/\text{H}\alpha$, suggesting that star formation could be contributing significantly among these. In the SDSS sample, we remove the 30% galaxies with the lowest $D_n(4000)$. This selection by $D_n(4000)$ rank is done separately in each redshift bin to take into account any potential aperture effects and redshift evolution. We choose a cut on $D_n(4000)$ rather than one based on line ratios to avoid biasing the comparison of emission line properties. In the rest of this paper, we refer to samples with possible star-forming galaxies removed as the Palomar red sample and the SDSS red sample.

To summarize, from the Palomar survey and SDSS, we identified a volume-limited sample of passive red galaxies without any star formation at $0 < z < 0.1$.

3. SPATIAL DISTRIBUTION OF LINE EMISSION

In this section, we investigate the spatial distribution of line emission. The spatial distribution alone does not distinguish between different ionization mechanisms, but it is essential for the interpretation of other measurements, such as line ratio gradients.

We do this in a two-step process. First, we compare the nuclear aperture measurements from the Palomar survey with the large aperture measurements from SDSS at $z \sim 0.1$ to establish the relation between nuclear LINERs in Palomar and the LINER-like galaxies in SDSS. Then, we utilize all apertures available to us from $0 < z < 0.1$ to measure the average emission line surface brightness profile among passive red galaxies.

3.1. Nuclear Emission vs. Extended Emission

In this section, we will compare the emission line luminosity distributions between two identically-selected, volume-limited samples, but for which the line luminosities are measured from different physical apertures. The difference in their luminosity distributions demonstrates that the emission measured in the larger aperture has to be spatially extended.

In the left panel of Figure 4, we compare $L(\text{H}\alpha)$ and $[\text{N II}]/\text{H}\alpha$ between the Palomar red sample and the SDSS red sample at $z \sim 0.1$. Not all galaxies in either sample have $\text{H}\alpha$ detected (64.4% of the Palomar red sample and 52.0% in the SDSS red sample at $z \sim 0.1$ have $\text{H}\alpha$ detection). Therefore, we only compare the brightest half of each volume-limited sample in $\text{H}\alpha$ luminosity.

The SDSS red sample shows much brighter $\text{H}\alpha$ luminosities and slightly lower $[\text{N II}]/\text{H}\alpha$ ratios than the Palomar sample. Since both samples are volume-limited to the same magnitude cut, we adopted the same sample selection, and any evolution effect over a redshift difference of 0.1 should be tiny, this difference in $\text{H}\alpha$ luminosities must be caused mostly by the difference in the physical aperture size between the Palomar survey and SDSS. The Palomar sample reflects the nuclear properties of red galaxies while the SDSS sample reflects their integrated properties on much larger scales.

The brightest 25th percentile in $\text{H}\alpha$ luminosity for the $z \sim 0.1$ SDSS sample (including non-detections) is $5.82 \times 10^{39} \text{ erg s}^{-1} h_{75}^{-2}$, nearly 7 times larger than that in the Palomar sample ($0.85 \times 10^{39} \text{ erg s}^{-1} h_{75}^{-2}$). In fact, even the median $\text{H}\alpha$ emitter in the SDSS red sample is brighter than the majority of nuclear $\text{H}\alpha$ emitters in the Palomar red sample. Nuclear emission in red galaxies is therefore only rarely as luminous as found in the SDSS galaxies. Furthermore, we expect no strong evolution in AGN activity between $z \sim 0.1$ and $z \sim 0$. Thus, in the SDSS galaxies, a substantial contribution to emission must come from outside the nucleus, and therefore the $\text{H}\alpha$ emission observed by SDSS in these $z \sim 0.1$ passive red galaxies has to be *spatially extended*.

One might wonder if the spatially extended emission found in large aperture measurements is due to low-level star formation in these galaxies. We can simulate the expected $[\text{N II}]/\text{H}\alpha$ ratio and $L(\text{H}\alpha)$ by adding a typical star-forming emission-line spectrum to a typical nuclear spectrum in the Palomar sample. We use the median $[\text{N II}]/\text{H}\alpha$ and median $\text{H}\alpha$ luminosity in the brighter half (in $\text{H}\alpha$) of the Palomar red sample to represent a typical nucleus. For star formation, we adopt an $[\text{N II}]/\text{H}\alpha$ ratio of 0.45, typical of a high metallicity star-forming galaxy, which yields a conservatively high $[\text{N II}]/\text{H}\alpha$ ratio. The result is shown by the curve in the left panel of Fig. 4. From the bottom end of the curve to the top, the $\text{H}\alpha$ luminosity contributed by the star formation goes from 0

to 100 times that of the typical nucleus. The curve misses the majority of the red galaxies at $z \sim 0.1$. Clearly, the spatially extended line emission in red galaxies we selected at $z \sim 0.1$ is not powered by star formation.

As described above, in constructing this passively-evolving red galaxy sample, we have removed potential star-forming contaminants by removing the 30% galaxies with the lowest $D_n(4000)$. The right panel of Figure 4 shows the effect of this procedure, where we plot the low $D_n(4000)$ galaxies plus those Palomar red galaxies with Hubble types later than S0 for comparison. In the SDSS, those red galaxies we have removed generally have higher $\text{H}\alpha$ luminosities and lower $[\text{N II}]/\text{H}\alpha$ than those we have kept do. For the right panel, the curve indicates the track traced by adding star formation to a typical passive red galaxy in the SDSS sample from the left panel. From the bottom end of the curve to the top, the $\text{H}\alpha$ luminosity contributed by star formation goes from 0 to 10 times that of the median $\text{H}\alpha$ luminosity in passive red galaxies at this redshift. The curve traces the distribution fairly well, suggesting that the line emission in red galaxies with low $D_n(4000)$ have more ongoing, low-level star formation than those red galaxies with high $D_n(4000)$.

The right panel of Fig. 4 also demonstrates that the Palomar red galaxies we have removed from the sample have fairly similar line luminosities and line ratios to those Palomar red galaxies we have kept (except for the three HII nuclei, with the lowest $[\text{N II}]/\text{H}\alpha$ ratios). This result reflects the fact that the Palomar spectra have smaller physical apertures. Therefore, although the criteria we used to remove star-forming contaminants differs slightly for the Palomar sample than for the SDSS sample, the Palomar sample is insensitive to these differences.

Now, we have shown that the line emission regions in passive red galaxies in SDSS have to be spatially extended, simply because few nuclear regions in red galaxies are luminous enough to explain the SDSS results. The next question is which galaxies host these extended $\text{H}\alpha$ emission regions at $z \sim 0$. Are they the same galaxies that host those nuclear emission regions? The answer must be “yes.” Suppose they were not the same galaxies: then galaxies hosting these extended $\text{H}\alpha$ emission regions would need to have undetectable line emission in their centers. No such galaxies are found by the SAURON survey. As shown by Sarzi et al. (2006), in a representative sample of 48 early-type galaxies in the nearby universe, all galaxies with emission lines detectable have their line flux peaking at the center, and the distribution is nearly always extended. Therefore, we conclude that most, if not all, red galaxies that have nuclear emission line regions also have extended line-emitting regions, and vice versa. The host galaxies of nuclear line emitting regions and those of extended line emitting regions are largely the same population.

3.2. Emission line surface brightness profile

In this section, we compare the emission line luminosity distributions among passive red galaxies at a series of redshifts, which translates to a series of apertures, to investigate the average surface brightness profile of their line emission. We bin the SDSS sample with $0.01 < z < 0.1$ into 9 redshift bins with a binsize of 0.01. We limit the

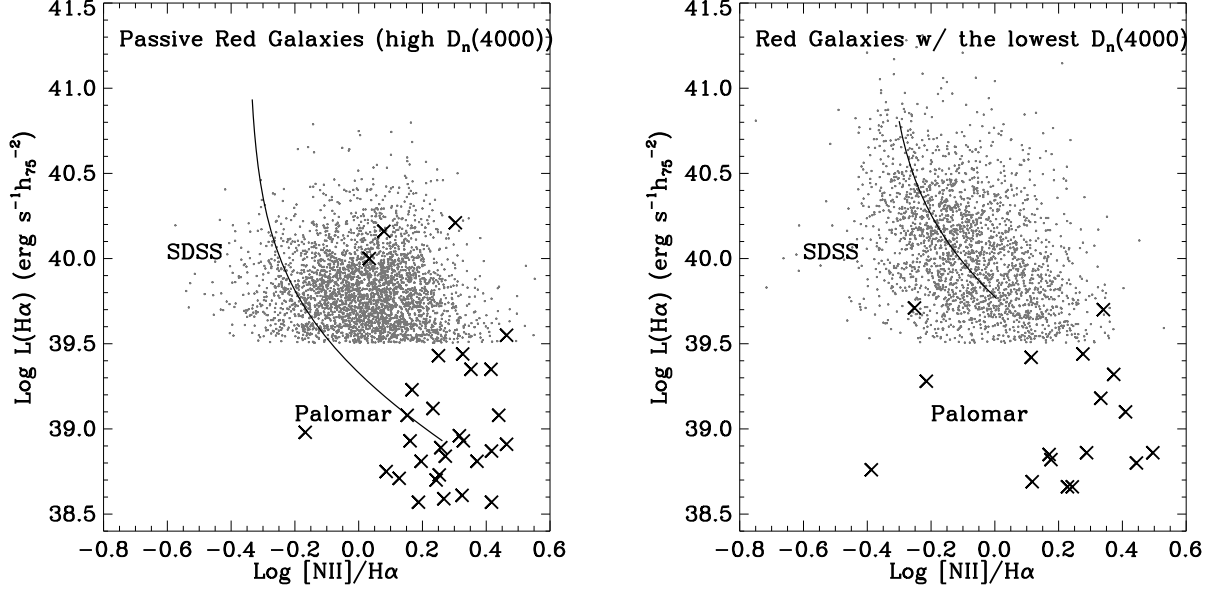


FIG. 4.— Left: $\log L(\text{H}\alpha)$ vs. $\log [\text{N II}]/\text{H}\alpha$ for passive red galaxies in the Palomar sample (dark crosses) and an SDSS comparison sample at $z \sim 0.1$ (gray points). Only the brighter half (in $\text{H}\alpha$ luminosity) of each sample is plotted, since the fainter half mostly have $\text{H}\alpha$ undetected. The Palomar data is measured from nuclear aperture spectra while the SDSS data is measured from spectra integrated on much larger scales ($5 h_{75}^{-1}$ kpc diameter). The curve represents the track followed by adding star formation to a typical Palomar nucleus. Clearly, star formation is not the cause of the luminosity difference. The much larger $\text{H}\alpha$ luminosities shown by the SDSS sample suggest that the line emission in them is spatially extended. The right panel shows the red galaxies that we have excluded from the left panel because of possible star formation contamination. For the SDSS, this means those red galaxies with the lowest $D_n(4000)$; for Palomar, this means those red galaxies with Hubble types later than S0 and those classified as HII nuclei by Ho et al. (1997a). The curve represents the track followed by adding star formation to a typical passive red galaxy in SDSS from the left panel. For the SDSS samples in both panels, we also excluded a small fraction (11% of the bright half in the left panel, and 1.5% in the right panel) of galaxies with poorly measured $[\text{N II}]/\text{H}\alpha$ ratios (with uncertainties larger than 0.25 dex), which has no practical impact on our conclusions.

Palomar sample to only those galaxies at $D < 40\text{Mpc}$, which corresponds to $z = 0.01$, for the lowest redshift bin.

Figure 5 shows the $\text{H}\alpha$ luminosity distribution as a function of redshift. In each bin, we only plot the brighter half of the sample in $\text{H}\alpha$. With increasing redshift, i.e., increasing aperture, the $\text{H}\alpha$ luminosities increase. Thus, the $\text{H}\alpha$ luminosities observed with larger apertures have to have significant contributions from spatially extended emission line regions. In each redshift bin, we sort all passive red galaxies by their $\text{H}\alpha$ luminosity. Figure 6 plots the brightest 25th percentile $\text{H}\alpha$ luminosity as a function of physical scale covered by the SDSS fiber. The 25th percentile is safely above the detection threshold at all redshifts. The luminosity increases with scale roughly as a power law with an index of 0.72, as shown by the power-law fit in Fig. 6. As this is the integrated luminosity within radius r , it indicates the average surface brightness profile follows $r^{-1.28}$. This slope is fairly consistent with what Sarzi et al. (2010) found in nearby early-type galaxies targeted by the SAURON survey (see their Figure 4). We also show the same measurement of the Palomar sample (with late-type galaxies removed) at the median effective radius probed by the $2'' \times 4''$ aperture in the Palomar survey, which we treat as equivalent to a circular aperture with $3''$ diameter. The 25th percentile in the Palomar sample is fairly consistent with the power-law fit to the SDSS data points. This evidence further strengthens the conclusion that the nuclear and the extended line emitting regions exist in the same galaxy

population.

However, the extended line emission alone does not constrain the source of the ionizing radiation. Contrary to intuition, the extended emission could also be produced by a central ionizing source, such as an AGN. The emission line brightness profile depends on many factors: the ionizing flux profile, the density profile, the gas filling factor, and how the typical size of the gas clouds change with radius. We leave the detailed calculations to §6.1.

4. LINE RATIO GRADIENT

With the above technique, we can also check if the line ratio distribution in this population changes between redshifts/apertures. This check can only be done on those galaxies with detectable line emission. To ensure low uncertainty on the line ratio measurement, we choose only the brightest 25% in total emission line luminosity at each redshift and compare their various line ratios. To avoid bias on the line ratios, instead of selecting the brightest 25% in $\text{H}\alpha$ luminosity, we base the selection on the total luminosity of the several strongest emission lines available in the spectra ($\text{H}\alpha + [\text{N II}] \lambda 6583 + [\text{O III}] \lambda 5007 + [\text{S II}] \lambda \lambda 6716, 6731$). This combination is a better proxy of the total line emission output than $L(\text{H}\alpha)$.

Figure 7 shows the full distribution of several line ratios as a function of aperture radius. We also plot those galaxies in the Palomar red sample with $D < 40\text{ Mpc}$ to probe the smallest scales. As for the SDSS sample, we only select the brightest 25% galaxies in total observed

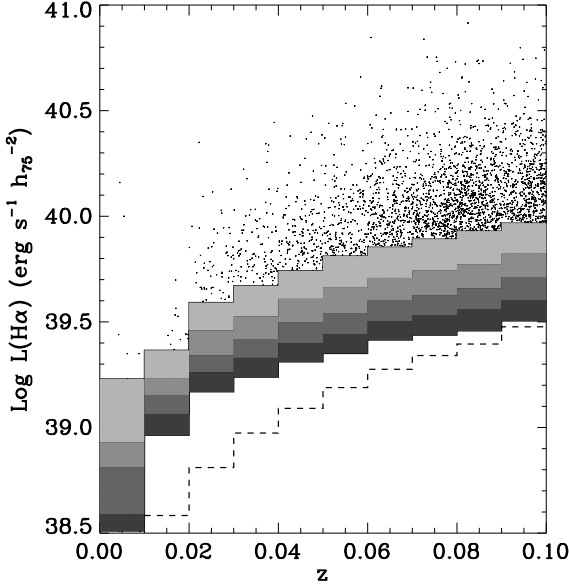


FIG. 5.— $H\alpha$ luminosity distributions of passive red galaxies as a function of redshifts. The first bin at $z < 0.01$ is from the Palomar sample and the rest are from the SDSS sample. Only the brighter half of the sample in each redshift bin is plotted. The brightest 10 percent of galaxies in $H\alpha$ in each bin are plotted as points. The gray scales indicate the ranges populated by different percentiles in each bin: brightest 10-20th, 20-30th, 30-40th, and 40-50th, from top to bottom, respectively. The dashed line at the bottom indicates the 3σ detection limit in SDSS, which is 3 times the luminosity corresponding to the median $H\alpha$ flux error in each bin. Clearly, the $H\alpha$ luminosity increases with increasing redshift or aperture size.

emission line luminosity.

Fig. 7 shows the distribution of line ratios in the red galaxies. At small aperture radii, the scatter is dominated by intrinsic variations in line ratios among galaxies. At the large aperture end, the uncertainty in line measurements starts to dominate the scatter, leading to a slight increase in the width of the distribution. In most line ratios, the intrinsic variation has a standard deviation of approximately 0.1 dex.

Interestingly, in some line ratios, the median of the distribution changes systematically with aperture radius, most notably in $[N II]/H\alpha$, $[S II]/H\alpha$, and $[O III]/[S II]$. The trends also extend to the Palomar sample at the smallest scales. The changes are so large in $[S II]/H\alpha$ and $[O III]/[S II]$ ratios that most of the Palomar sample populates only one side of the median of SDSS sample even in its first bin.

Figure 8 shows how the median line ratios change with aperture size, with the error bars giving the uncertainties of the median estimates. The systematic changes in $[N II]/H\alpha$, $[S II]/H\alpha$, and $[O III]/[S II]$ with radius are significant and the Palomar sample confirms the trend on small scales.

One might worry that the change in $[O III]/[S II]$ ratio could be due to dust extinction, because these two lines are separated in wavelength. However, the $H\alpha/H\beta$ ratio is nearly constant with radius, indicating that the average dust extinction does not vary much. The values of the median $H\alpha/H\beta$ ratio are also close to the Case B

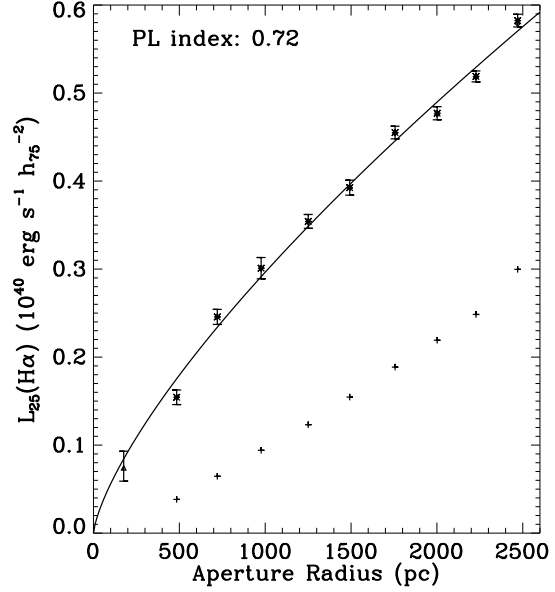


FIG. 6.— The 25th percentile (counting from the brightest) $H\alpha$ luminosity (asterisks with error bars) measured with SDSS fibers in a sample of non-star-forming red sequence galaxies as a function of the physical scale probed by the fiber. The triangle point represents the measurement in the Palomar sample, which is fairly consistent with the extrapolation of the power-law fit on small scales. The uncertainties of these measurements are measured with bootstrap resampling. The '+' signs at the bottom indicate the 3σ detection limits.

prediction of 2.85 (or 3.1 if collisional excitation is included), indicating that the level of dust extinction is low. Applying extinction corrections to each galaxy in the sample only shifts the median $[O III]/[S II]$ ratio up by a nearly constant ~ 0.1 dex in each bin.

The line ratios presented in Fig. 8 are cumulative measurements: they reflect the luminosity-weighted average line ratios within aperture radius r , rather than that in an annulus at radius r . We need to combine these median line ratios in integrated apertures with the median line luminosity of this sample in corresponding apertures, to derive the average line ratios in circular annuli at radius r .

In Fig. 9, we show the median line luminosities of this sample in corresponding apertures for $H\alpha$, $[S II]$, and $[O III]$. This plot is similar to Fig. 6, but uses only the 25% brightest galaxies in total emission line luminosity. From this figure, it is evident that the $[S II]$ line has a very different surface brightness profile from $H\alpha$ and $[O III]$, consistent with the trends in integrated line ratios.

With the integrated line ratios and integrated luminosities, we can compute the line ratio in annuli. For example, the average $[N II]/H\alpha$ ratio between radius r_i and r_j can be computed by the following equations,

$$\left\langle \frac{[N II]}{H\alpha} \right\rangle_{r_i < r < r_j} = \frac{\left\langle \frac{[N II]}{H\alpha} \right\rangle_{r < r_j} L_j(H\alpha) - \left\langle \frac{[N II]}{H\alpha} \right\rangle_{r < r_i} L_i(H\alpha)}{L_j(H\alpha) - L_i(H\alpha)}, \quad (3)$$

where $L_i(H\alpha)$ and $L_j(H\alpha)$ are the median luminosities in apertures with radius r_i and r_j , respectively. The

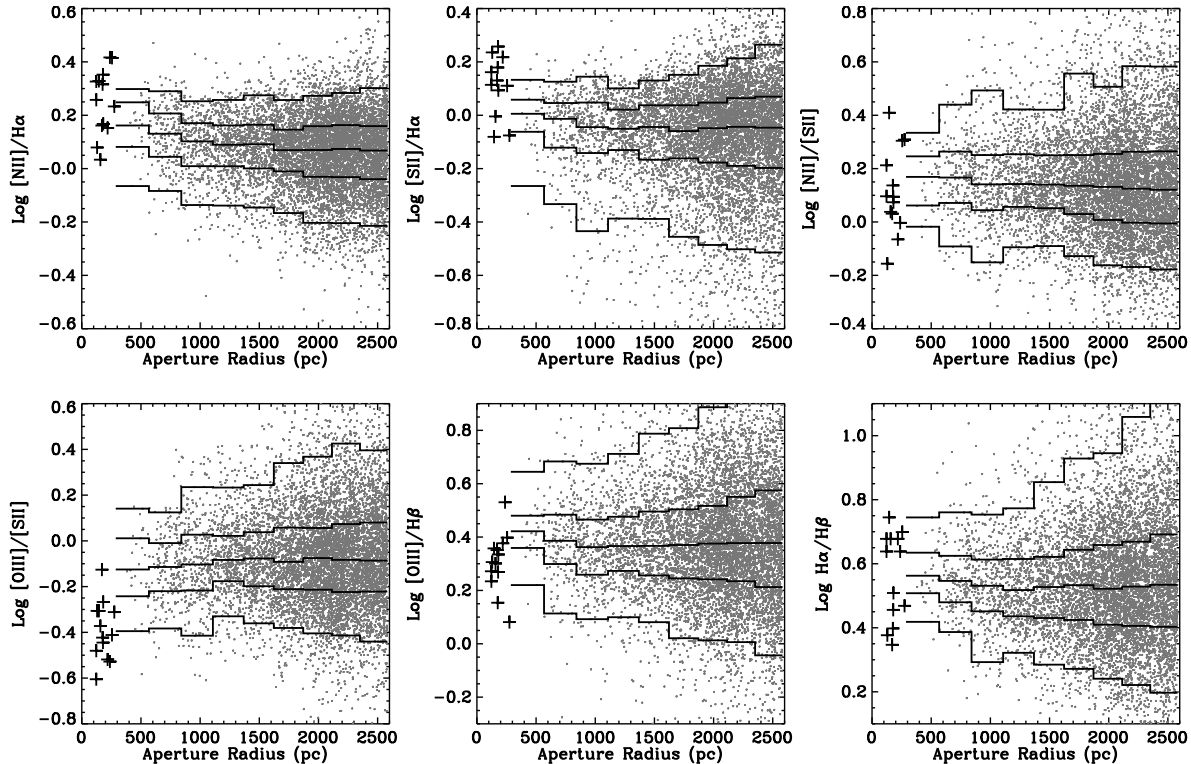


FIG. 7.— Integrated line ratio distribution as a function of the aperture radius for passive red galaxies in SDSS (gray points) and the Palomar sample (red crosses). The line ratios are “integrated” in the sense that they are derived using the fluxes interior to the indicated aperture radii. Only the 25% brightest (in $H\alpha$) galaxies in each redshift bin are plotted to ensure small uncertainty on the line ratio measurement. The lines indicate the 5-, 25-, 50-, 75-, 95-percentile points in each redshift bin. The aperture of Palomar galaxies are computed using an effective radius of $1.5''$.

$[S II]/H\alpha$ and $H\alpha/H\beta$ ratios in annuli are also computed by combining integrated line ratios with the median $H\alpha$ luminosities. The $[N II]/[S II]$ and $[O III]/[S II]$ ratios are computed by combining integrated line ratios with the median $[S II]$ luminosities. The $[O III]/H\beta$ ratios are computed by combining with the median $[O III]$ luminosities. Calculating this between every consecutive bin results in large uncertainties, due to the large fractional error in the luminosity differences. We therefore calculate the annulus line ratios using aperture pairs: $[i, j] = [1, 3], [1, 4], [2, 5], [3, 6], [4, 7], [5, 8], [6, 9], [7, 10],$ and $[8, 10]$, where Aperture 1 is the Palomar aperture and Aperture 10 is the aperture for SDSS galaxies at $0.09 < z < 0.1$. The results are shown in Fig. 10

Although the uncertainties become much larger, the differences between the innermost bin and the outer bins remain robust in $[N II]/H\alpha$, $[S II]/H\alpha$, and $[O III]/[S II]$. The second bin in each panel always shows a very large uncertainty. This is due to the dramatic change in line ratios between the first few bins and their larger uncertainties. In Table 1, we list the line ratios of the inner most bin and the median line ratios of the outer bins ($700 < r < 2500$ pc).

The line ratio gradients we observe have been in principle detectable in past long-slit spectroscopic surveys of early-type galaxies (e.g., Phillips et al. 1986; Kim 1989; Zeilinger et al. 1996; Ho et al. 1997a; Caon et al. 2000). However, these authors either did not have data with sufficient quality or did not look at the line ratio gradient at all. The only exception is Zeilinger et al. (1996), who

TABLE 1
MEDIAN LINE RATIOS WITHIN 300 PC RADIUS AND OUTSIDE 700 PC

Location	$\log[N II]/H\alpha$	$\log[S II]/H\alpha$	$\log [O III]/[S II]$
Inner 300 pc	0.25 ± 0.03	0.13 ± 0.04	-0.40 ± 0.04
Outside 700 pc	0.01 ± 0.01	-0.07 ± 0.01	-0.07 ± 0.01

showed that the $[N II]/H\alpha$ ratio decreases outwards in four galaxies. However, like many of these past surveys, their data did not have wide enough wavelength coverage to cover multiple line ratios, which would be critical for identifying the cause of the line ratio gradients. Recently, Annibali et al. (2010) investigated the line ratio gradients using long-slit spectra with wide wavelength coverage for a sample of relatively gas-rich early-type galaxies. They found that the $[N II]/H\alpha$ ratios in most of them decrease with radius, consistent with our result. However, they did not look for gradients in other line ratios, except for $[O III]/H\beta$, which is very often too noisy to support firm conclusions.

We will discuss in §6 what changes in physical conditions are required to produce such changes in line ratios.

5. CLUES FROM LINE WIDTHS

We initially thought that the line ratio gradient would produce different line widths in different emission lines, due to varying kinematics of the line emitting clouds across each galaxy. If this were so, it could provide a complementary constraint on the radial distribution of

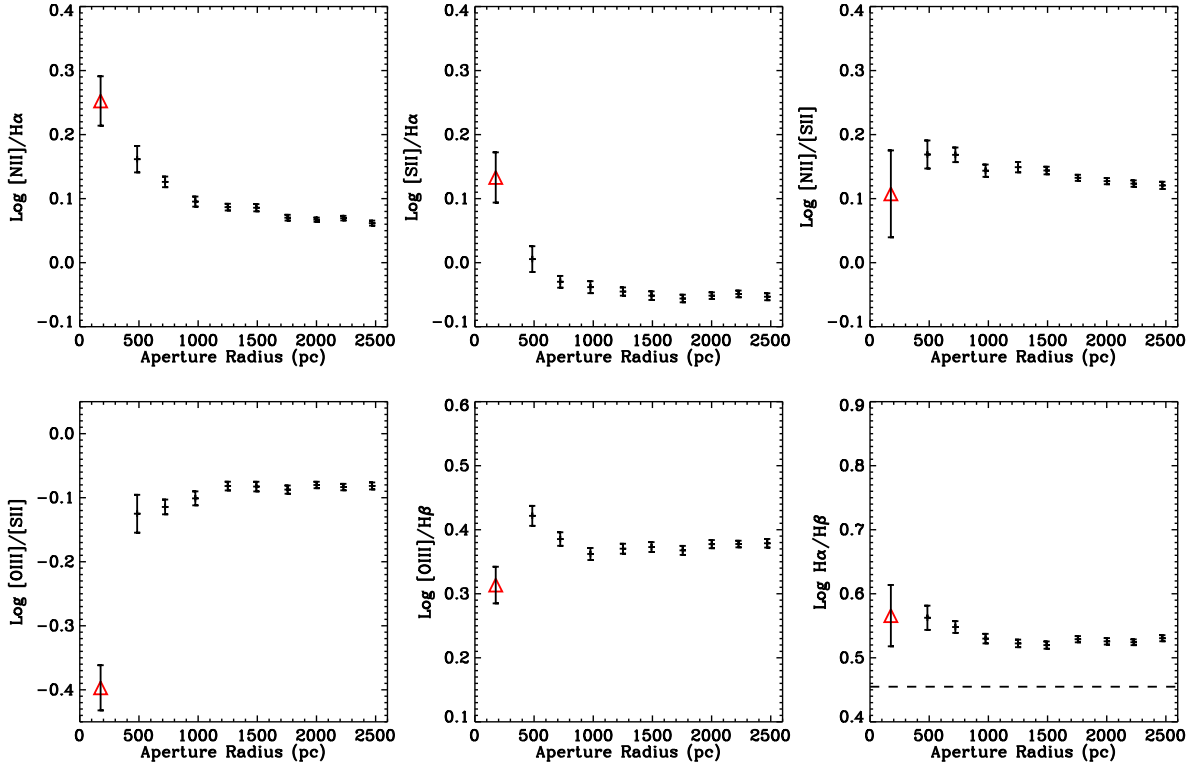


FIG. 8.— Median integrated line ratios as a function of aperture radius for the 25% brightest line emitters among the red galaxies in SDSS (> 300 pc) and the Palomar sample (< 300 pc). For the median, we use the biweight center estimator (Beers et al. 1990), which is more robust than the median for small samples. The uncertainty is given by the jackknife error of the biweight estimator. All panels cover 0.5 dex in y-axis for the ease of comparison. The horizontal line in $H\alpha/H\beta$ panel marks the Case B ratio of 2.85.

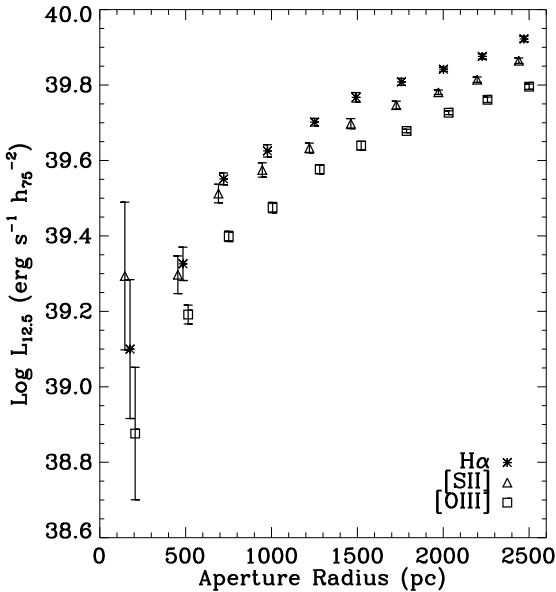


FIG. 9.— The median integrated $H\alpha$ (asterisk), $[S II]$ (triangle), and $[O III]$ (square) luminosities as a function of aperture among the 25% passive red galaxies (in each bin) with the brightest total emission line luminosity. The smallest scale is probed by the Palomar sample and the larger scales are probed by the SDSS sample. The $[S II]$ and $[O III]$ points are slightly shifted in the horizontal direction for clarity. The uncertainties of these measurements are measured with bootstrap resampling.

the emission. The data do indeed show different line widths for different lines. However, we have concluded that this variation is probably not due to line ratio and kinematic gradients, primarily because the line width differences are not a function of aperture size. We describe our investigation of line width differences in this section.

Because the width measurement is noisy on SDSS spectra, we need a control sample to demonstrate that our line width measurement is robust. The star-forming galaxies provides such a comparison. In a pure star-forming galaxies, the line emission originates mostly from HII regions photoionized by O and B stars. The line width in integrated spectra reflects the rotation velocity of the galaxy. In the absence of strong metallicity gradient, we would observe approximately the same line ratios in all HII regions. In this case, all lines should display the same line width.

We choose a star forming galaxy sample using the line ratio criteria described by Kewley et al. (2006). Basically, the galaxies in this sample are selected to fall in the star-forming branch on all three diagnostic diagrams ($[O III]/H\beta$ vs. $[N II]/H\alpha$, $[S II]/H\alpha$, and $[O I]/H\alpha$). We compare this star-forming galaxy sample with the sample we used for deriving the line ratio profile, namely the top 25% passive red galaxies that have the highest total emission line luminosities in each redshift bin. We combine all the redshift bins together. In addition, to ensure good measurements on the line width ratio, we require the uncertainty of the line width ratio to be smaller than 0.1 dex.

In Figure 11, we plot the distributions of width ratio

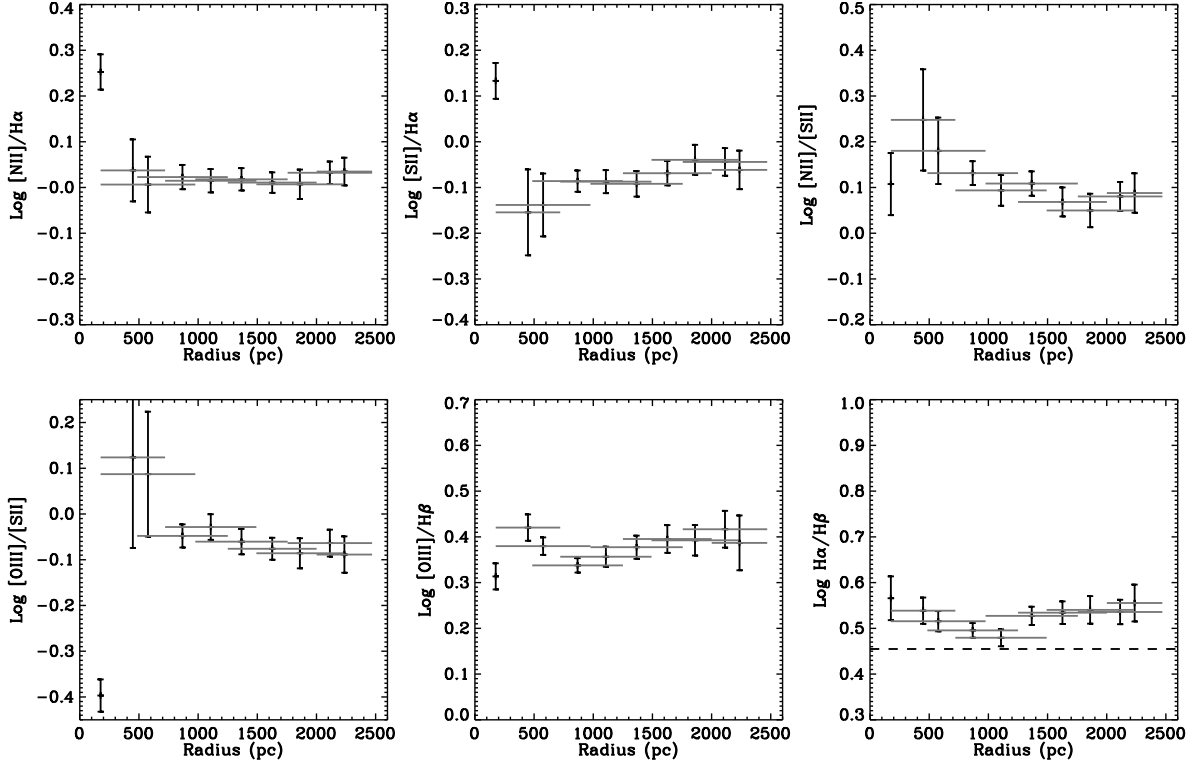


FIG. 10.— Average line ratios in annuli as a function of radius for passive red galaxies. This is derived by combining the integrated line ratios in Fig. 8 with the integrated luminosities in Fig. 9, through equations similar to Eqn. 3. The horizontal bar of each data point indicates the range of radius covered by the annulus. Note the y-axis in each panel covers a larger range (0.7 dex) than Fig. 8.

in four line pairs for galaxies in the star-forming sample (thin-lined histograms) and in the passive red galaxy sample (thick-lined histograms). In all line pairs, the distribution of star-forming galaxies always show a fairly symmetric and narrow distribution peaking around zero in logarithmic space, meaning all the lines have roughly the same width. This proves that our line width measurement is robust. It also indicates that line ratios in star-forming HII regions do not correlate strongly with the velocity of the HII regions. The [O III]-to-[S II] pair may be an exception; for star-forming galaxies this width ratio has a wider distribution than the other line pairs. This broad distribution probably reflects intrinsic variation in the population. It might be caused by variation in the disturbed component of the diffuse ionized medium in star-forming galaxies, which produces strong and wide [O III] lines (Wang et al. 1997). We leave this question for future investigations.

However, for line-emitting passive red galaxies, the distributions in [N II]-to-[S II], [O III]-to-[S II], [S II]-to-H α width ratios do not peak around zero in log space. Their offsets from zero are highly significant. On average, the [N II] and H α lines in them are wider than [S II] lines by 8% and the [O III] lines are wider than [S II] by 16% (Table 3). This means the [O III]/[S II] ratios in the line wings are higher than that in the line center, and the higher velocity clouds which contribute to the wings must have higher [O III]/[S II] ratios. The same must be true for [N II]/[S II] and H α /[S II] ratios. This indicates that in these galaxies, line emitting clouds do not have uniform line ratios and the line ratio must correlate with the

velocity of the clouds.

In the previous section, we found the line ratios have a systematic variation with radius. Could these line ratio variations produce the line width differences?

Given the fact that [O III]/[S II] ratio increases with radius, to obtain a wider [O III] line than [S II], the line-of-sight velocity broadening must also increase with radius. The broadening could either come from random motions or ordered rotation. As shown by previous long slit (Phillips et al. 1986; Kim 1989; Zeilinger et al. 1996) and IFU (Sarzi et al. 2006) observations, in most early-type galaxies, the kinematics of the gas is largely consistent with disk-like rotation with rotation velocity increasing outwards (though see Heckman et al. 1989 for some exceptions). This is consistent with the requirement here. The [N II]-to-[S II] and [S II]-to-H α width ratios could also be consistent with their respective line ratio gradients (if the decrease in [N II]/[S II] towards the center is real, as indicated by the Palomar data point). However, the [N II] show the same width as H α , inconsistent with the expectation.

On the other hand, if the width difference is indeed caused by the line ratio gradient and the rotation of the gas disk, the line width difference should get smaller in larger apertures, since we expect the flux to be increasingly dominated by the outskirts where the line ratio profile gets flat. Figure 12 shows the line width ratio distributions as a function of aperture radius. Apparently, the average line width ratios are roughly constant, independent of the aperture size. This is inconsistent with the expectation of the model.

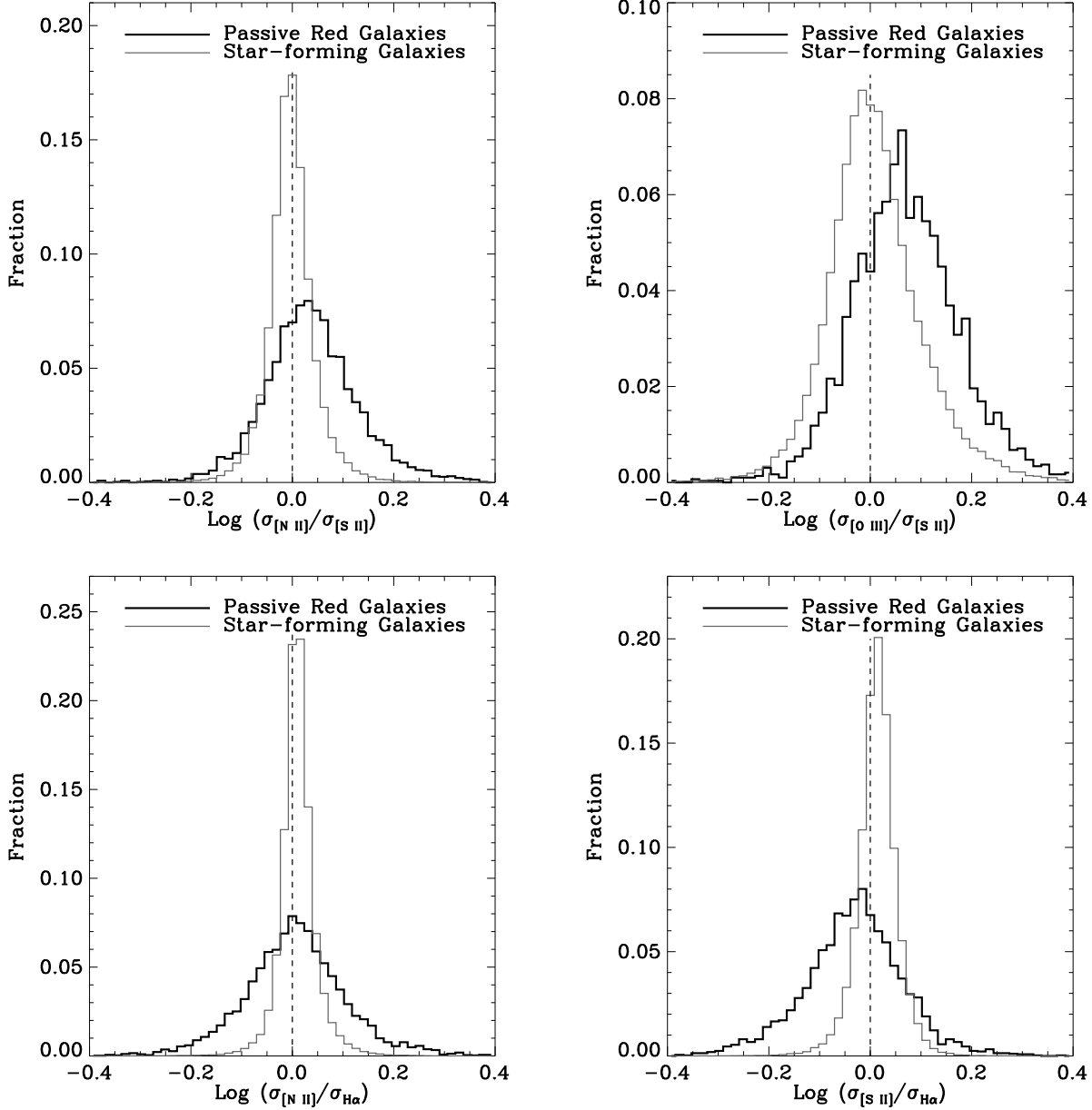


FIG. 11.— Panel (a): Distributions of line width ratio between [N II] and [S II] for star-forming galaxies (thin-lined histogram) and passive red galaxies (thick-lined histograms). [N II] in passive red galaxies are systematically wider than [S II] in both samples. Panel (b), (c), (d) show the same comparisons in [O III]-to-[S II] width ratio, [N II]-to-H α width ratio, and [S II]-to-H α width ratio, respectively.

We demonstrate this inconsistency quantitatively by simulating the expected line width ratios using a toy model of a rotating gas disk in a spherically-symmetric galaxy with stellar mass of $7.5 \times 10^{10} M_{\odot}$ and an effective radius of 4.8 kpc, the median values among our 25% passive red galaxy sample with the brightest total line luminosity. The rotation curve of the gas disk is set by the stellar density profile, which is assumed to be a γ -model described by Dehnen (1993) with $\gamma = 1.5$. This stellar density profile gives a stellar surface brightness profile closely resembling the de Vaucouleurs' $R^{1/4}$ profile. The integrated luminosity profile in [O III] is fixed to be a power law with index of 0.77, measured by fitting the data points in Fig. 9. The inclination of the disk is

set at 60° . We assume that the line ratios at each point in the disk are solely dependent on radius. We model the logarithm of the line ratio profile as a broken power-law of the form,

$$\log \frac{[\text{O III}]}{[\text{S II}]} = \begin{cases} A(r/r_0)^{\gamma_1} - 0.5 & , r < r_0 \\ (A - 0.4)(r/r_0)^{\gamma_2} - 0.1 & , r \geq r_0 \end{cases} \quad (4)$$

Based on the trend seen in Fig. 10, we fix the model to have $\log [\text{O III}]/[\text{S II}]$ equal to -0.5 (an arbitrary choice) at $r = 0$ and asymptote to -0.1 as $r \rightarrow \infty$. We fit the model to the integrated line ratios rather than the differentiated line ratios, since the former have independent uncertainties.

The velocity dispersion in the disk is assumed to be a

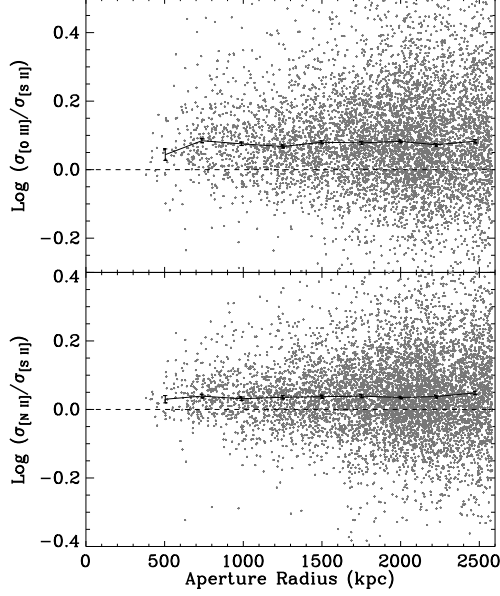


FIG. 12.— Top panel: the [O III]-to-[S II] width ratio distribution as a function of aperture radius for the 25% passive red galaxies with the highest total line luminosity. The dark points with error bars indicate the median width ratio in each redshift bin. Bottom panel: same plot for the width ratio between [N II] and [S II].

TABLE 2
LINE-RATIO PROFILE MODEL PARAMETERS

A	r_0 (kpc)	γ_1	γ_2
1.86	345.9	3.69	-2.44
1.56	309.2	3.82	-2.04
1.21	402.3	2.29	-1.98
0.982	565.1	1.30	-2.30
0.868	364.7	1.58	-1.46

constant everywhere and equal to 50kms^{-1} . Many gas kinematic studies have shown that the velocity dispersion is likely to increase towards the center. Here we assume the extreme case of flat dispersion, since using an increasing velocity dispersion towards the center would erase the line width differences.

We employ a Markov-Chain Monte Carlo technique to find a large number of models that best fit the data. Among the 10 data points, we ignored the second bin ($r \sim 500$ pc) in the fitting, as including it makes the fit difficult. We chose five typical but different models to illustrate the trend expected in line width differences as aperture radius increases. The model parameters are given in Table. 2.

The left panel of Fig. 13 shows these models give reasonably good fits to the integrated line ratio profiles. The right panel of Fig. 13 shows the line width ratio as a function of aperture radius for these models. The solid curves and the dashed curves show the result for two different methods for measuring the line width. Because circular rotation makes more boxy profiles than Gaussian, the width measured from Gaussian fitting is different from that measured from FWHM. No matter how the width is measured, the width ratio between [O III] and [S II] pro-

TABLE 3
MEDIAN LINE WIDTH RATIOS

Line pair	Star-forming galaxies	Old red galaxies
$\sigma[\text{N II}]/\sigma[\text{S II}]$	0.991 ± 0.0004	1.079 ± 0.004
$\sigma[\text{O III}]/\sigma[\text{S II}]$	1.006 ± 0.001	1.164 ± 0.006
$\sigma[\text{S II}]/\sigma\text{H}\alpha$	1.033 ± 0.0004	0.933 ± 0.004
$\sigma[\text{N II}]/\sigma\text{H}\alpha$	1.022 ± 0.0003	1.009 ± 0.003

duced by all circular rotation models decreases strongly towards large apertures, inconsistent with what we observe. The decrease in width ratio towards large aperture is expected in the model since the line luminosity is increasingly dominated by flux from large radius and the line ratio profile flattens outward. Therefore, the line width ratio is probably not caused by the line ratio gradient and circular rotations. So, what is the real cause of the line width difference?

The line width is mainly contributed by two components: the thermal broadening and the bulk motion of the clouds. For gas at $T = 10^4\text{K}$, the thermal broadening is approximately 15km/s for $\text{H}\alpha$. For the red galaxies in our sample, the lines are very wide, with Gaussian sigmas ranging between 100km/s and 300km/s and a median of 176km/s in [N II] lines. Therefore, the thermal broadening is a minor contributor. The width is likely dominated by bulk motion broadening or turbulence in the clouds.

To produce a width difference between different lines, we have to have clouds with different line ratios and different line widths, and the line ratio has to correlate with the line width. For example, for [O III] and [S II] to have different widths, we need a population of clouds with high [O III]/[S II] flux ratio and a population of clouds with low [O III]/[S II]. To make a wider [O III] than [S II], those high [O III]/[S II] clouds need to produce a wider width than those low [O III]/[S II] clouds. Basically, to produce a constant width ratio with radius, the width ratio has to be approximately the same everywhere in the galaxy. Thus it requires at least two components of the ISM throughout the galaxy that have different line ratios and different line broadening. Because the total flux ratio has a gradient with radius, the two components need to have approximately synchronous line ratio gradient behaviours. One component is kinematically more disturbed than the other and thus produces a wider line width. Our observed width ratios indicate that the more disturbed component has higher [O III]/[S II] and [N II]/[S II] ratios, lower [S II]/ $\text{H}\alpha$ ratio, and similar [N II]/ $\text{H}\alpha$ ratio to the more quiescent component. Without knowing the ionization mechanism for the gas, the origin of these multiple components and the reason for their line ratio difference is difficult to analyze.

We check if the line width difference changes with the line strength. Figure 14 shows the width ratio distribution between emission lines as a function of $\text{H}\alpha$ EW. We only use the brightest 25% galaxies in total emission line luminosity and excluded among them those with uncertainty on line width ratio greater than 0.2 dex. The median [O III]-to-[S II] and [N II]-to-[S II] width ratios always stay above 1. The [O III]-to-[S II] width ratio seems to decrease slightly with increasing $\text{H}\alpha$ EW.

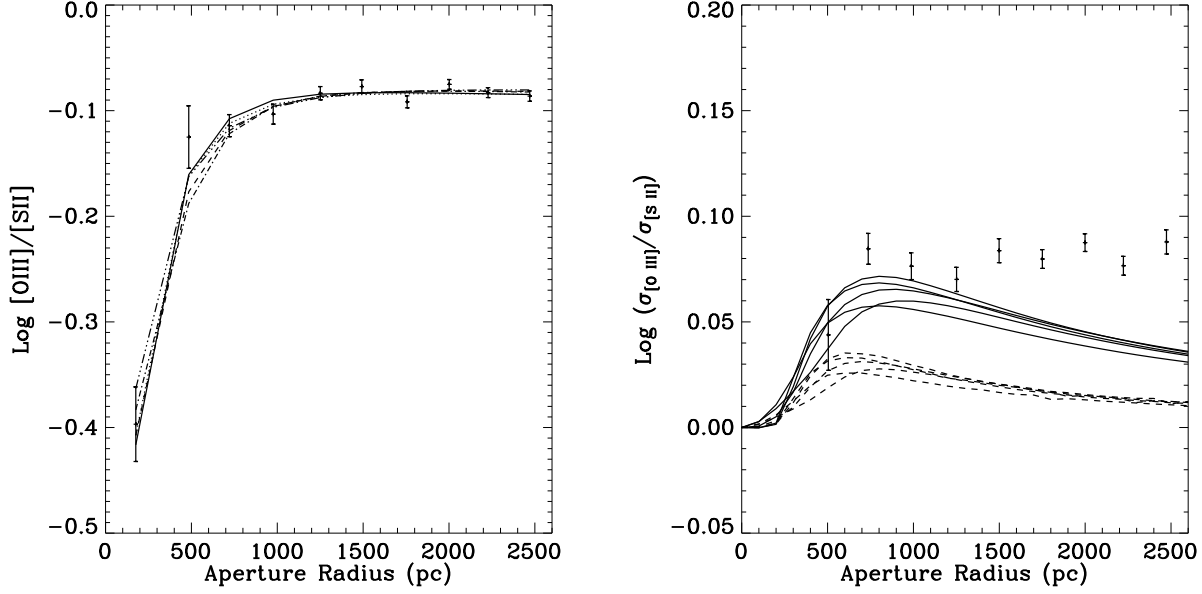


FIG. 13.— Left panel: $[\text{O III}]/[\text{S II}]$ line flux ratio as a function of aperture radius for the data (points with error bars) and a few simple models. Right: The $[\text{O III}]$ -to- $[\text{S II}]$ width ratio as a function of aperture radius for the data and the models. The two sets of curves indicate line widths measured by different methods, with solid lines indicate FWHM ratios and dashed lines indicate ratios from Gaussian fits. The models assume thin gas disk in circular rotation, with flat velocity dispersion.

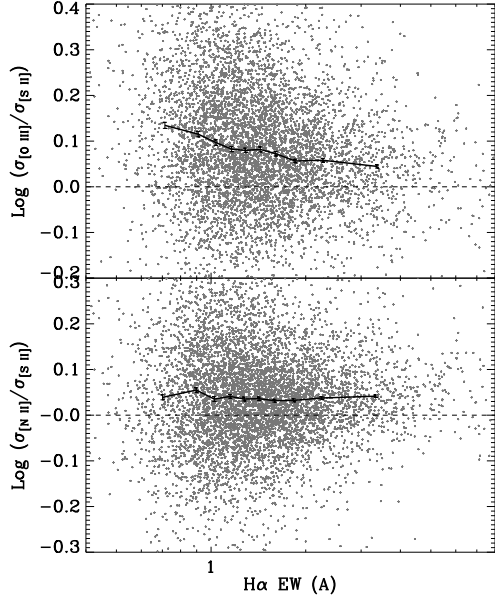


FIG. 14.— Top panel: the width ratio distribution between $[\text{O III}]$ and $[\text{S II}]$ as a function of $\text{H}\alpha$ EW for line-emitting red galaxies. Bottom panel: same plot for the width ratio between $[\text{N II}]$ and $[\text{S II}]$.

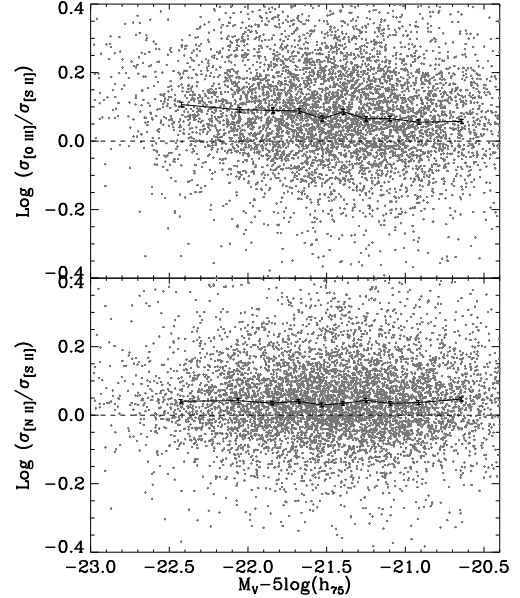


FIG. 15.— Top panel: the width ratio distribution between $[\text{O III}]$ and $[\text{S II}]$ as a function of luminosity for line-emitting red galaxies. Bottom panel: same plot for the width ratio between $[\text{N II}]$ and $[\text{S II}]$.

Figure 15 show the width ratio distribution for the line-emitting red galaxies as a function of absolute luminosity. The same sample is used as in Fig. 14. The $[\text{N II}]$ -to- $[\text{S II}]$ width ratio stays flat as a function of luminosity but the $[\text{O III}]$ -to- $[\text{S II}]$ width ratio declines slowly towards fainter galaxies. The important point is that they always show significant offset from zero in log space, suggesting that the reason causing the width difference

is universal in these galaxies.

6. DISCUSSION

In this section, we first discuss what physical factors determine the emission line surface brightness profile, and show that the profile alone does not provide a discriminator between different ionization mechanisms. Then, we discuss the viability of the different ionization

mechanisms in light of the observational results we presented above.

6.1. Surface Brightness Profile

Except shock heating and conductive heating by the hot gas, all other major ionization mechanisms proposed involve photoionization. In this section, we consider a generic photoionization model and examine which of its parameters determine the emission line surface brightness profile.

We assume that the ISM is filled with hot, ionized gas. Embedded in it are neutral dense clouds. Each cloud is optically-thick to the ionizing radiation. In photoionization equilibrium, for each cloud the total emission line luminosity has to be equal to the total photoionizing luminosity it receives, which is the incoming flux times the projected area of the cloud. Therefore, the luminosity density profile depends on the photoionizing flux profile (as a function of radius) and the total projected cloud area per unit volume. For example, for a volume filling factor of f_g , assuming the clouds have an average volume of $\langle V \rangle$ and an average projected area of $\langle A \rangle$, the luminosity density of line emission would be

$$j(r) = F(r) \frac{f_g(r)}{\langle V \rangle} \langle A \rangle \quad (5)$$

Here, $F(r)$ is the ionizing flux profile. The second term on the right hand side gives the number density of clouds. Multiplying it with the average projected area yields the total projected cloud area per unit volume. To obtain the final surface brightness profile, we also need to convolve the luminosity density profile with the spatial distribution of the clouds. If the clouds all reside in a disk with constant thickness, then the surface brightness scales with radius in the same way as the luminosity density. However, if the thickness of the disk increases with radius, like the Milky Way gas disk, then the surface brightness profile would be much shallower. Assuming the scale height of the disk is $H(r)$, the surface brightness of the line emission would be

$$\Sigma(r) = F(r) f_g(r) H(r) \frac{\langle A \rangle}{\langle V \rangle} \quad (6)$$

The typical cloud area and volume could also change with distance from the center. Because the gas density (n) depends on distance from the galaxy center, if the mass distribution of the clouds is independent of the distance, then the typical $\langle A \rangle / \langle V \rangle$ will scale as $n^{1/3}$. Therefore, the constraint from the surface brightness profile is

$$\Sigma(r) = F(r) f_g(r) H(r) n^{1/3} \propto r^{-1.28} \quad (7)$$

We do not have enough information about the geometry of the cloud distribution and how the typical cloud sizes change with radius to constrain the photoionizing flux profile. Therefore, the extended line emission only provides a partial constraint on the source of the ionization. We need more information from other methods.

Many ionization mechanisms have been proposed to explain the observed emission line ratios in these red galaxies, which mostly have LINER-like line ratios. In the following sections we consider these mechanisms, dividing them generically into three categories: a central

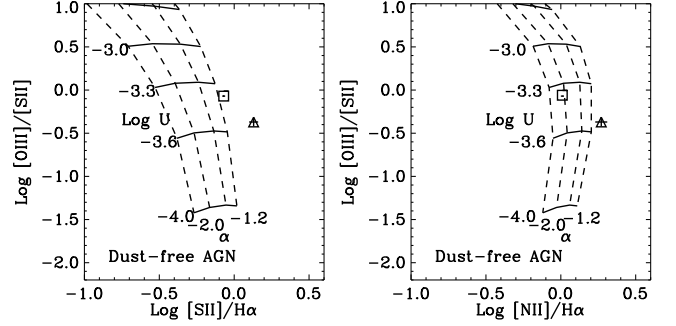


FIG. 16.— Line ratio diagnostic diagrams for the center (triangle) and outskirts (square) of passive red galaxies, overlaid on the MAPPINGS III models of a classical dust-free AGN photoionization model. The models assume a metallicity of $2Z_{\odot}$ and a hydrogen density of 1000 cm^{-3} . The solid lines indicate constant ionization parameters ($\log U = -4.0, -3.6, -3.3, -3.0$) and the dashed lines indicate constant spectral indices ($\alpha = -2.0, -1.7, -1.4, -1.2$).

photoionizing source, distributed photoionizing sources, and shocks.

6.2. Photoionization by an accreting SMBH

An accreting supermassive black hole will emit X-rays and extreme UV radiation that photoionizes surrounding gas clouds and produces line emission. In this section we will examine the predictions of this model for the line ratio gradients and line width differences.

6.2.1. Line ratio gradients for a SMBH

First, we will demonstrate that this model cannot explain the observed line ratio gradients. To do so, we use models calculated with the MAPPINGS III codes (Dopita & Sutherland 1996; Groves et al. 2004a; Allen et al. 2008). Figure 16 shows two line ratio diagnostic diagrams with the grids representing the models presented by Groves et al. (2004a).

This standard photoionization model (with no dust or radiation pressure) assumes a metallicity of $2Z_{\odot}$ and a hydrogen density of 1000 cm^{-3} . With the given range of parameters, this model cannot produce the $[\text{S II}]/\text{H}\alpha$ and $[\text{N II}]/\text{H}\alpha$ ratios observed in the center of these galaxies. In fact, none of the dust-free classical models in Groves et al. (2004a) can produce the central $[\text{S II}]/\text{H}\alpha$ ratio: they are all too low. It may be possible to fit the $[\text{S II}]/\text{H}\alpha$ ratios by tweaking the N/S abundance ratio, or adopting the dusty, radiation-pressure dominated photoionization model (Dopita et al. 2002). However, it is unlikely that the latter model is applicable to the low intensity radiation fields in LINERs.

Since we are not yet certain about the ionization mechanism, it is premature to constrain the exact physical parameters using these measurements. However, the models should provide a guide as to the direction of change in the line ratios. Thus, we only use these models to investigate what the line ratio gradients tell us about the change in the physical parameters, not their precise values.

The line ratios are primarily determined by four parameters: gas density (n), metallicity (Z), ionization parameter ($\log U$)³, and the spectral index (α). From the

³ U is the dimensionless ratio of the ionizing photon flux density

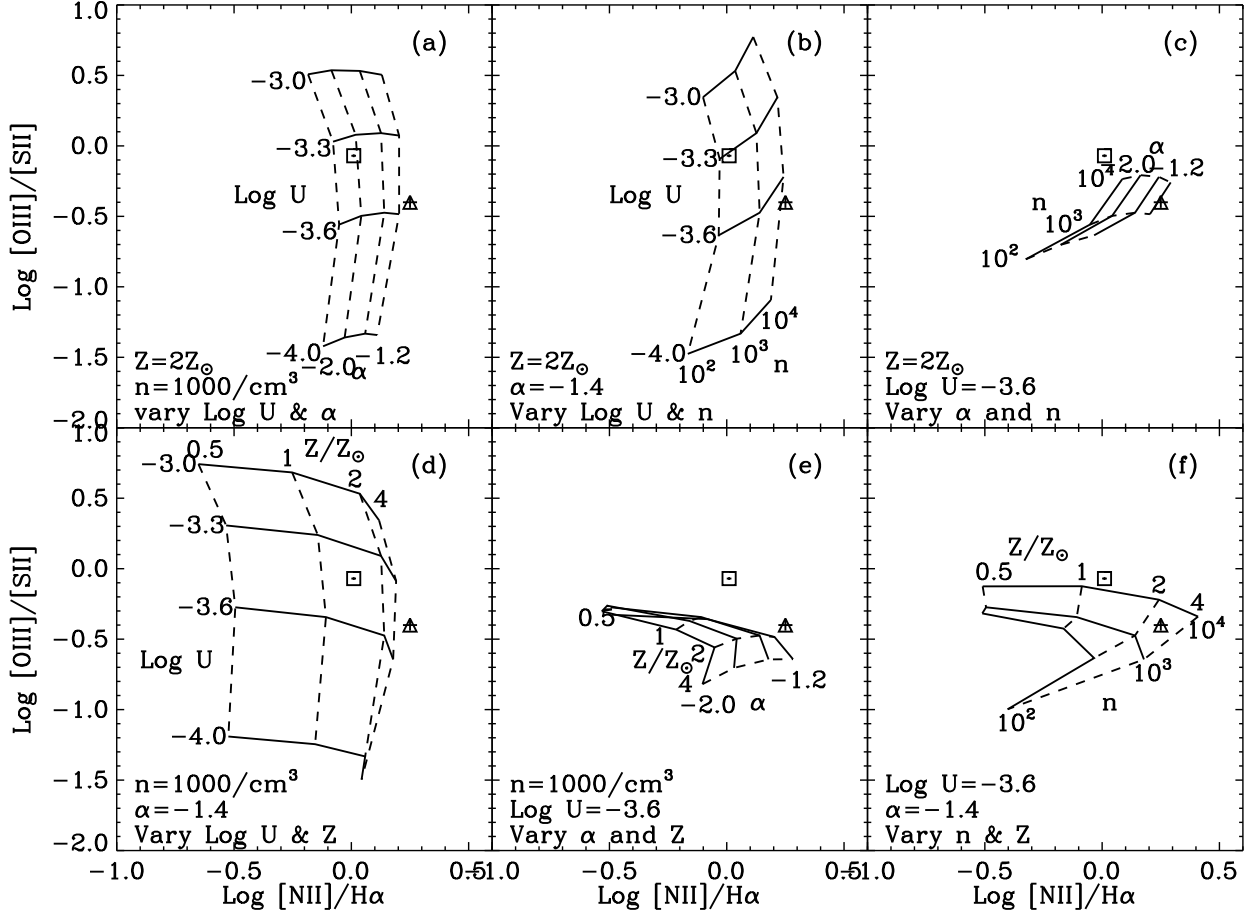


FIG. 17.— $[\text{O III}]/[\text{S II}]$ vs. $[\text{N II}]/\text{H}\alpha$ for the classical dust-free AGN photoionization models (grids) and the measurements at the center (triangle) and outskirts (square) of line-emitting red galaxies. We explore the dependence of line ratios on four parameters: ionization parameter ($\log U$), spectral index (α), gas density (n), and metallicity (Z). In each panel, we fix two parameters and vary the other two to see how the line ratios depend on each parameter.

four strong lines, $[\text{S II}]$, $[\text{N II}]$, $\text{H}\alpha$, $[\text{O III}]$, we have only three line ratios at each position. Therefore, we cannot hope to determine the trend in all of these parameters and have to start by keeping some parameters fixed. In the six panels of Fig. 17, we fix two parameters at a time and look at the line ratio dependence on the other two parameters, to determine all possible scenarios for the observed line ratio variation. We only look at $[\text{O III}]/[\text{S II}]$ vs. $[\text{N II}]/\text{H}\alpha$ diagram since the $[\text{S II}]/\text{H}\alpha$ data points are not well covered by the models.

There are three ways that the $[\text{O III}]/[\text{S II}]$ ratio can increase outward: an increase in the density (panel c), a decrease in the metallicity (panel d), or an increase in the ionization parameter (panel a). For the first option, it is unphysical to expect the density to increase outwards, which would require a higher gas pressure at larger radius (since the temperature in the ionized gas is likely to be always near 10^4K).

The second option, the metallicity gradient, is also not a likely source for the change in $[\text{O III}]/[\text{S II}]$ ratio. At fixed density and ionization parameter, it requires a factor of ~ 3 change in metallicity with radius, which is com-

parable though somewhat larger than the observed stellar metallicity gradients (Kuntschner et al. 2010). However, the density is likely to decrease outwards, which acts as a countervailing force and would require a larger metallicity gradient. Indeed, since at low metallicity the $[\text{O III}]/[\text{S II}]$ ratio becomes insensitive to Z , this possibility could be ruled out.

The third option, an increasing ionization parameter, is much more promising. $[\text{O III}]/[\text{S II}]$ is quite sensitive to $\log U$: a variation of more than 0.1 dex would dominate any other possible effect. Even before considering specific models, we should suspect that the ionization parameter in these objects increases outwards.

The ionization parameter is defined as the ratio between ionizing flux and gas density. Therefore, we now examine how gas density changes with radius. X-ray observations of giant ellipticals have shown that the hot gas density follows the square root of the stellar density profile, $n_e \propto \rho_*^{1/2}$ (Mathews & Brighenti 2003 and references therein). This means that the gas density profile falls with radius as r^{-p} with $0.5 < p < 1$ at the center and an increasing p at large radii. This range of central density slope is consistent with the more recent X-ray measurements by Allen et al. (2006). The temperature profile of

to the electron density, $U \equiv q(H^0)/(cn_H)$.

the hot gas is much flatter, varying by at most 50% between the center and the outskirts (Mathews & Brighenti 2003). The gas clouds that generated the observed optical line emission always have temperature near 10^4K . Therefore, under pressure equilibrium, with the nearly constant temperature profile in both the hot gas and the warm ionized gas, the density in the warm ionized gas clouds should fall with radius in roughly the same way as the hot gas density.

It is important to note that this density scaling is only verified in giant ellipticals. In fainter early-type galaxies it may not hold. Nonetheless, we expect the central density profile in faint ellipticals is also much shallower than $1/r^2$. Evidence for this comes from density profile measurements in the central regions ($\lesssim 100\text{pc}$) of a few fainter early-type galaxies (NGC 1052, NGC 3998, NGC 4579) from [S II] line ratios. Walsh et al. (2008) showed that the power-law indices of their gas density profiles are around -0.6 . Therefore, we use the $n_e \propto \rho_*^{1/2}$ scaling as a working assumption here and in the next section. Our main conclusion remains the same if one switches to a power law density profile with $n_e \propto r^{-1}$ or shallower.

In the case of a central ionizing source, the flux decreases as r^{-2} . Since the gas density is at most decreasing as r^{-1} , the ionization parameter must decrease outwards by a large amount, at least 0.5 dex. No change in metallicity or spectral index could conceivably make up for this decrease: this model inevitably predicts a strongly decreasing [O III]/[S II] ratio with radius, the opposite of what we observe. Therefore, unless the gas density profile actually falls faster than r^{-2} , the AGN photoionization model cannot explain the observed line ratio gradients.

Meanwhile, there are also three ways for the [N II]/H α ratio to decrease outward: a softening of the ionizing spectrum (panel a), a decrease in the density (panel b), a decrease in the metallicity (panel d), or a combination of these. The outward decreasing density provides a natural solution. Though its decline with radius might be too slow to explain all the change in [N II]/H α ratio. An additional contribution from metallicity gradient and a change in the spectral index might be needed as well. With the current modeling uncertainty, we cannot break the degeneracy among these possibilities.

6.2.2. Comparison to line width differences observed in nearby Seyferts

Next, we consider the observed variations of line width between our various lines. We conclude here that the variations we observe are probably not related to those known to exist for Seyfert galaxies.

Velocity width variations among different emission lines have been observed in classical nearby Seyferts and LINER nuclei (Filippenko & Halpern 1984; Filippenko 1985; De Robertis & Osterbrock 1986; Ho et al. 1996). In most cases, the line widths correlate strongly with critical density for collisional deexcitation: lines with higher critical density tend to have larger widths. In a minority of Seyfert 2s, the line width correlates with the ionization potential of the ions.

The line width differences we observe for LINERs is broadly consistent with that seen in local Seyferts. In a sample of 18 Seyfert 2 galaxies presented by

De Robertis & Osterbrock (1986), the median of [N II]-to-[S II] width ratio is 1.11 ± 0.06 , the median of [O III]-to-[S II] width ratio is 1.18 ± 0.08 . Our width ratios are only slightly smaller.

Filippenko & Halpern (1984) proposed the following picture to explain the line width differences. The ionization flux decreases outward according to the inverse-square law. If the density also falls as r^{-2} , then the ionization parameter seen by each cloud will be the same. If all clouds are optically-thick to the ionizing radiation, then they will all have the same ionization structure and produce the same set of emission lines. The relative line ratio will vary according to the density of each cloud. Lines with a high critical density will be mainly contributed by a high density clouds, which are closer to the nucleus and have higher velocities.

In this scenario, the [N II]/[S II] and [O III]/[S II] flux ratios should increase towards the center, the opposite of what we observe for LINERs. In addition, for most red galaxies the line emission is spatially extended, with an average surface brightness profile falling as $r^{-1.28}$. Thus, the line luminosity is not dominated by the central regions where the density gradient is steep. The kinematic structure on large scales is also different from the Keplerian rotation found near the SMBH. Therefore, while the scenario is applicable to the narrow line regions of Seyferts, cannot be applicable in our case. The similar line width ratios of our results and those of De Robertis & Osterbrock (1986) may simply be a coincidence.

6.3. Photo-ionization by Distributed Ionizing Sources

The suggestion that the ionization parameter increases outwards naturally points to a slower decrease in the flux and thus to distributed ionizing sources rather than a central one. A number of models have been proposed along these lines, such as photoionization by hot evolved stars and by the hot X-ray emitting gas. In this section we first discuss the generic predictions of models with distributed sources, and then discuss particular models in more detail.

6.3.1. Line ratio gradients from distributed sources

Although the ionizing spectra produced by these models differ from that produced by an AGN, the overall dependence of line ratios on ionization parameter and metallicity are very similar. Thus, as in the case of AGN, to explain the line ratio gradients we need the ionization parameter to increase outwards. Distributed sources can produce this trend.

Suppose the ionizing sources are distributed like the stars, i.e., their luminosity density profile follows the stellar density profile. Then, we can compute the ionizing flux profile using the latter. Assuming that the galaxy is spherically symmetric, that the stellar density profile is $\rho(r)$, and that the average number of output photoionizing photons per unit time per unit stellar mass is Q_0 , the total integrated ionizing flux at distance D from the center of the galaxy is:

$$F(D) = \int_0^\infty dr \int_0^{2\pi} d\phi \int_0^\pi \frac{Q_0 \rho(r) r^2 \sin \theta}{4\pi(D^2 + r^2 - 2Dr \cos \theta)} d\theta \quad (8)$$

$$= \frac{Q_0}{2} \int_0^\infty \rho(r) \frac{r}{D} \ln \frac{D+r}{|D-r|} dr \quad (9)$$

The integral can be solved by substituting $r = D(1+e^u)$ for the $r > D$ part and substituting $r = D(1-e^u)$ for the $r < D$ part.

For the stellar density profile, we adopt the γ -model described by Dehnen (1993):

$$\rho(r) = \frac{(3-\gamma)M}{4\pi} \frac{a}{r^\gamma(r+a)^{4-\gamma}} \quad (10)$$

where M is the total mass, and a is a scaling factor which relates to the effective radius R_e , depending on the inner slope, γ . The $\gamma = 1$ model corresponds to the Hernquist (1990) profile, the $\gamma = 2$ model corresponds to the Jaffe (1983) profile, and the $\gamma = 1.5$ yields the best approximation of the de Vaucouleurs' $R^{1/4}$ model in surface brightness profile. Putting this model in Eqn. 9, we integrate numerically to obtain the total ionizing flux as a function of radius for a model galaxy with an effective radius of 4.8 kpc and a stellar mass of $7.5 \times 10^{10} M_\odot$, the medians for the top 25% line-emitting passive red galaxies in our sample.

Figure 18 shows the resulting ionizing flux profile for three models with different γ values, along with the inverse square law expected from a central ionizing source. In the inner kpc, distributed ionizing sources will produce a much shallower ionizing profile than the inverse square law.

In Figure 19, we divide the ionizing flux profiles by a gas number density profile to see how the dimensionless ionizing parameter will vary with radius under these different models. We adopt a gas density profile that scales as the square root of the stellar density profile, $n_g \propto n_*^{1/2}$ (Mathews & Brighenti 2003 and references therein, also see discussion in §6.2.1), and normalize them to 100 cm^{-3} at 1 kpc. This warm gas density is consistent with observations (Heckman et al. 1989; Donahue & Voit 1997) and our assumption of pressure equilibrium between the warm gas ($T \sim 10^4 \text{ K}$) and the hot gas ($T = 10^6 - 10^7 \text{ K}$, $n = 0.1 - 1 \text{ cm}^{-3}$). Interestingly, for the $\gamma = 1.5$ model, which gives the best fit to de Vaucouleurs' profile, the ionizing parameter displays the same trend as we observe, as shown by the $[\text{O III}]/[\text{S II}]$ ratio profile in Fig. 10. It not only produces the increase with radius in the central part but also a slow decline on the outskirts.

6.3.2. Luminosity dependence

A prediction of the above model is that the line ratio gradient should have a luminosity dependence. Many studies (Lauer et al. 1995; Faber et al. 1997; Rest et al. 2001; Ravindranath et al. 2001; Lauer et al. 2005; Ferrarese et al. 2006; Glass et al. 2011) have shown that the inner power-law slope of the stellar luminosity density profiles changes from -1 for bright galaxies to -2 for faint galaxies. As shown by Figure 19, these different stellar density profiles should generate different gradients

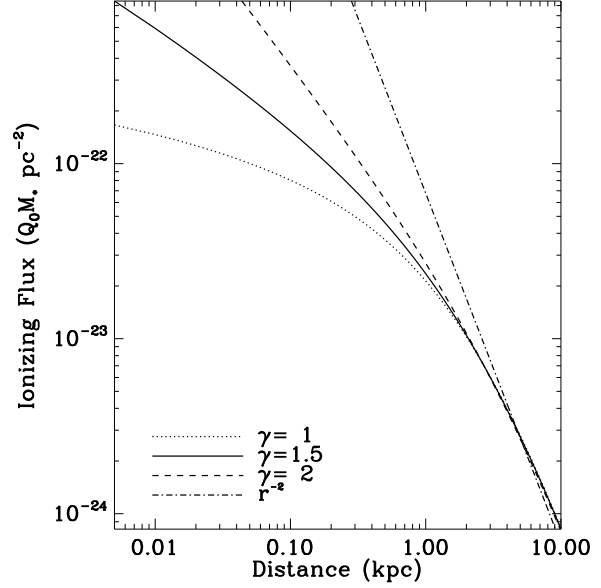


FIG. 18.— The integrated ionizing flux from a system of ionizing sources following the stellar density profile as a function of distance to the center of a model galaxy. The curves correspond to different γ -models for the stellar density profile. The solid line corresponds to the model with the best fit to the de Vaucouleurs' profile in surface brightness. The long dashed line corresponds to the inverse square law as expected in the AGN model. All models show flatter flux profile.

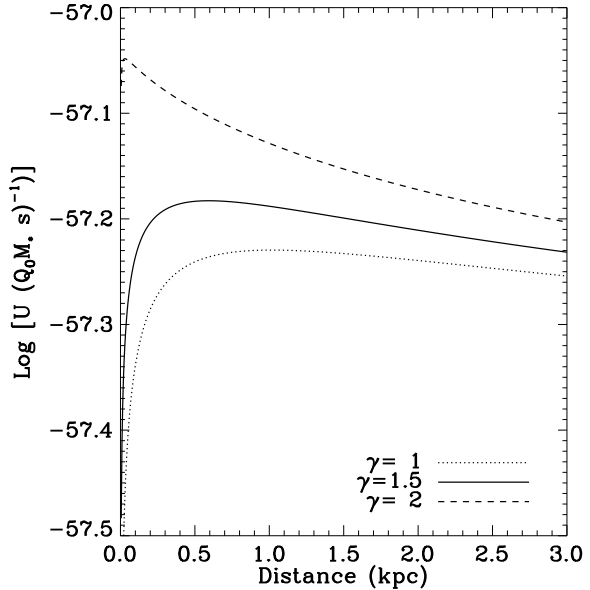


FIG. 19.— The ionization parameter produced by a system of ionizing sources following the stellar density profile in a galaxy shining a cloud as a function of distance from the galaxy center. We assumed gas density profiles of $n(r) \propto n_*^{1/2}$ and normalize them to 100 cm^{-3} at 1 kpc. The three curves correspond to three different γ -models as described by Eqn. 10. M_* is the stellar mass of the galaxy.

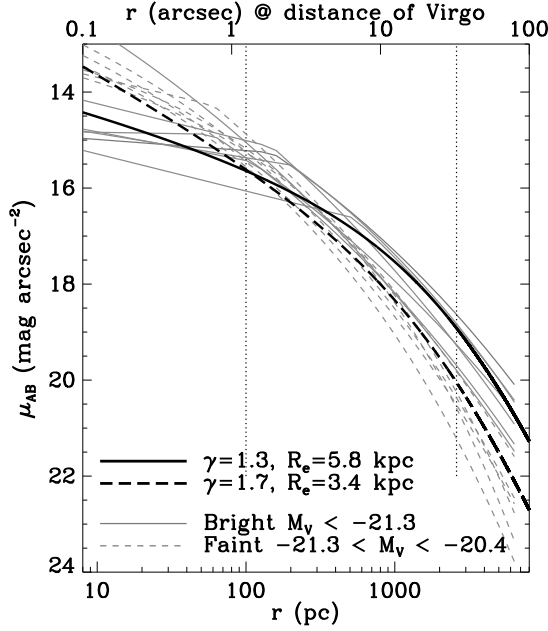


FIG. 20.— Surface brightness profiles for the 14 early-type galaxies in the Virgo cluster that would satisfy our luminosity cut ($M_V < -20.4$), as fit by Ferrarese et al. (2006). The solid gray curves and the dashed gray curves represent galaxies brighter and fainter than M_V of -21.3 , respectively. The two thick curves represent the profiles computed for two Dehnen (1993) models, with parameters indicated in the legend. They provide reasonable approximations to the profile difference between bright and faint early-type galaxies. The two vertical dotted lines indicate the range of apertures probed in this paper.

in the ionization parameter. The transition point is approximately at $M_B = -20.5$ (or around $M_V = -21.3$). Here, we investigate whether the gradients depend on luminosity in the expected manner.

We divide our passive red galaxy sample at $M_V = -21.3$ into bright and faint samples to look for the luminosity dependence. The bright sample has a median stellar mass of $1.0 \times 10^{11} M_\odot$ and a median effective radius of 5.8 kpc. For the faint sample, the corresponding numbers are $4.7 \times 10^{10} M_\odot$ and 3.4 kpc.

First, we show that Dehnen (1993) models with different γ values can provide reasonable approximations to the density profiles of bright and faint galaxies in our sample. To demonstrate this, we compare the models to the surface brightness profile fits presented by Ferrarese et al. (2006) for the 14 early-type galaxies in the Virgo cluster that satisfy our luminosity cut ($M_V < -20.4$). In Fig. 20, the gray solid curves show profiles of the brighter galaxies with $M_V < -21.3$ and the gray dashed curves show those of the fainter ones. The fainter galaxies generally have steeper profiles, despite their smaller Sersic indices as reported by Ferrarese et al. (2006). The difference can be reasonably approximated by the difference between the surface brightness profiles of two Dehnen (1993) models with $\gamma = 1.3$, $R_e = 5.8$ kpc, and with $\gamma = 1.7$, $R_e = 3.4$ kpc.

Next, we demonstrate that the shape of integrated ionization parameter profile is not sensitive to the effective radius of the galaxy, but is primarily controlled by the γ parameter. Bright galaxies not only have shallower inner density profiles, but also have larger effective radii than

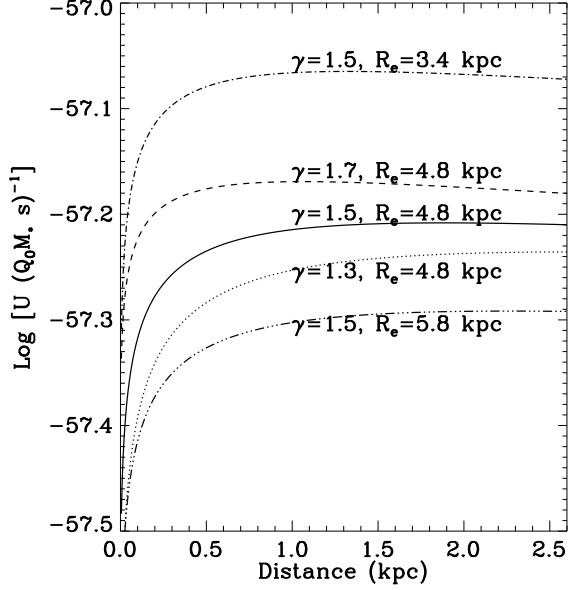


FIG. 21.— Luminosity-weighted ionization parameter within aperture as a function of aperture radius, for five models with different stellar density profiles. The density profiles are specified by its inner power-law slope, γ , and effective radius, R_e . The gas density are assumed to scale as the square root of the stellar density and is normalized to 100cm^{-3} at 1 kpc for all models. This figure shows that γ controls the shape of the resulting ionization parameter profile while R_e affects mainly the normalization.

faint galaxies. In Figure 21, we plot models with various choices for γ and R_e . The ionization parameter plotted is the luminosity-weighted average within an aperture. For the luminosity weighting, we assume a power-law surface brightness profile with an index of -1.23 , as derived from a fit to the [O III] profile in Fig. 9⁴. Combined with the ionization parameter profile from the model, we compute the luminosity-weighted average ionization parameter as a function of aperture radius. In all models, the gas density is assumed to scale as the square root of the stellar density and they are all normalized to be 100cm^{-3} at 1 kpc.

The middle three curves in Fig. 21 are models with the same $R_e = 4.8$ kpc but different γ . They have different slopes in both the outer part and the inner part. They differ little in overall normalization. The top and bottom curves have the same γ as the solid curve, but differ in R_e . These three cases have nearly identical shapes, but differ significantly in their normalization. Other factors can impact the normalization, including Q_0 , the stellar mass, and the normalization of the gas density. Without knowing Q_0 and the normalization of the gas density, the normalization of the curve is free to vary. In contrast, only γ controls the shape of the ionization parameter profile. Since we know γ varies with luminosity, a definite prediction by this model is that the bright sample and faint sample should differ in the shape of their integrated [O III]/[S II] profile.

Now we check this luminosity dependence in the data.

⁴ The data show that the line emission surface brightness profile has only a weak dependence on the galaxy luminosity. Thus, we adopt the same luminosity profile for all models.

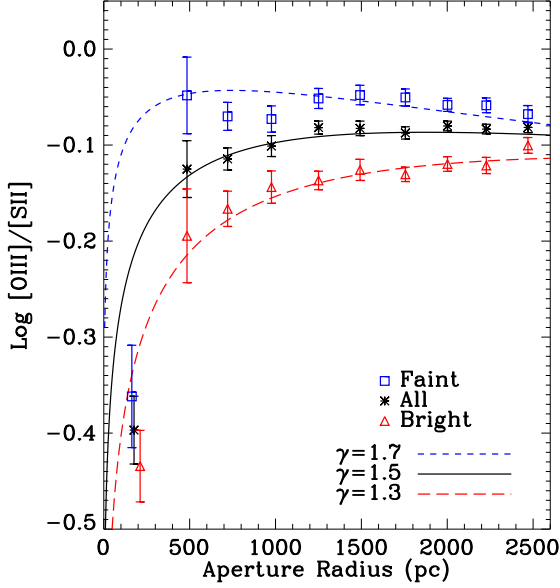


FIG. 22.— The aperture $[\text{O III}]/[\text{S II}]$ ratio as a function of aperture size for the whole sample (stars), bright sample (triangles, $M_V < -21.3$), and faint sample (squares, $M_V > -21.3$). The curves represent predictions of three simple models with different γ parameter (Eqn. 10). They are *not* fits to the data, but a scaled and shifted version of the luminosity-weighted average ionization parameter. See text for detail.

We divide all passive red galaxies into bright and faint subsamples at $M_V = -21.3$. As in the whole sample, we select the top 25% galaxies in each subsample that have the brightest total emission line luminosity. Figure 22 shows the $[\text{O III}]/[\text{S II}]$ ratios as a function of aperture size for the bright sample and the faint sample separately, along with those for the whole sample. The curves represent the prediction of three models with different γ parameter, R_e and stellar mass, with the latter two parameters adopting median values in the data. The models are calculated in the same way as for Fig. 21.

To convert the luminosity-weighted average ionization parameter, we used the median stellar mass and R_e for each model, assumed that Q_0 was constant, and assumed that every 0.3 dex in $\log U$ translates to 0.5 dex in $[\text{O III}]/[\text{S II}]$ ratios. Then we shifted the models vertically by varying the gas density normalization so that the $\gamma = 1.3, 1.5$, and 1.7 models match roughly the normalization of the data points for the bright sample, the whole sample, and the faint sample, respectively. We did not perform an explicit fit using these data because there are still too many poorly-known factors in the model. Under our assumptions, the gas density at 1 kpc must be $\sim 13\%$ lower for the faint sample than in the full sample, and $\sim 6\%$ higher for the bright sample. This normalization difference between the bright and faint samples does not have to be due to a density difference. It could also be due to the higher fraction of flat systems (lenticular galaxies) in the faint sample (Bernardi et al. 2010). The stars in an intrinsically flat galaxy would be systematically closer to the gas and yield a larger ionization parameter, hence higher $[\text{O III}]/[\text{S II}]$ ratios.

Although the normalizations match the data by de-

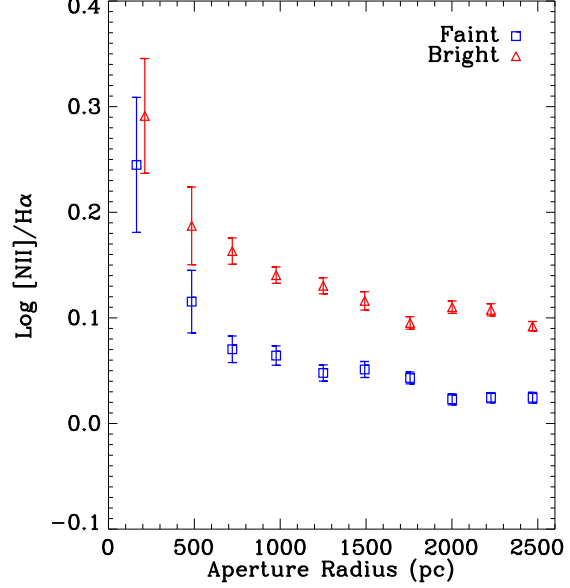


FIG. 23.— Aperture $[\text{N II}]/\text{H}\alpha$ ratios for the bright (triangles) and faint (squares) passive red galaxies as a function of aperture radius.

sign, the shape of the models are set completely by the γ values. The bright galaxy sample has an increasing $[\text{O III}]/[\text{S II}]$ ratio (integrated) with radius, matching the model prediction of a stellar density profile with a flatter inner slope (small γ). The faint galaxies have a much flatter outer slope, matching the prediction by a stellar profile with a steeper inner slope (large γ). In addition, the fainter sample displays a much steeper line ratio gradient on small radii (< 500 pc) than the brighter sample, matching the general trend predicted by the model.

The data on the smallest scales do not match the data. This mismatch could be due to the overly simplified assumptions we made. The scaling between $[\text{O III}]/[\text{S II}]$ ratio and $\log U$ may be non-linear; the inner gas density profile may be steeper than assumed. These could all change the shape of the curves.

It is remarkable that a simple single-parameter model is able to predict the overall luminosity dependence of the $[\text{O III}]/[\text{S II}]$ profile shape in the data. It provides a strong support for ionization mechanisms invoking sources that are distributed like the stars.

In Fig. 23, we show the $[\text{N II}]/\text{H}\alpha$ ratios as a function of aperture size for the bright and faint samples. The brighter sample always shows larger median $[\text{N II}]/\text{H}\alpha$ ratios than the fainter sample. This correlation between $[\text{N II}]/\text{H}\alpha$ and galaxy luminosity has been seen by Phillips et al. (1986). Our result shows that this correlation exists at all aperture scales. As we learned from Fig. 17, to increase $[\text{N II}]/\text{H}\alpha$ with photoionization, we have to either increase the metallicity, increase the density, or use harder ionizing spectra. The density is unlikely to vary by more than a factor of 10 between the bright galaxies and faint galaxies. And if all galaxies are powered by the same ionizing sources, the spectra should also be the same. Therefore, the difference in $[\text{N II}]/\text{H}\alpha$ is most likely due to the gas-phase metallicity difference between the two samples.

To summarize, photoionization by distributed ionizing sources following the stellar density profile can naturally produce the general variation of ionization parameter with radius, including the sharp rise at small radius and gentle decline on large radius. It is also able to produce the overall direction of the luminosity-dependence of the line ratio gradient. This strongly indicates that the spatial distribution of the true ionizing source is similar to the stellar distribution.

6.3.3. Post-AGB stars

Binette et al. (1994) proposed that photo-ionization by post-AGB stars could explain the extended line emission in red galaxies. The spatial distribution of these post-AGB stars should be very similar to the overall stellar distribution. Therefore, based on the results of the previous sections, the diffuse ionizing field they form can produce the observed line ratio gradient and its luminosity dependence. In this section we discuss relevant aspects of post-AGB evolution and planetary nebulae, and evaluate whether they can produce enough ionizing photons and a sufficiently high ionization parameter.

These stars have left the asymptotic giant branch and are evolving horizontally on the H-R diagram towards very high temperatures ($\sim 10^5\text{K}$) before cooling down to form white dwarfs. They are burning hydrogen or helium in a shell around a degenerate core. Because their temperatures are high enough to ionize the surrounding medium and plenty of material has been expelled from them in earlier evolutionary stages, they are often accompanied by a planetary nebula. After their planetary nebulae disperse into the interstellar medium, the long-lived post-AGB stars can produce a diffuse ionizing field.

Most of our knowledge about post-AGB stars comes from studies of planetary nebulae. Observations of planetary nebulae have shown their dynamical ages are about 30000 years (Schoenberner 1983; Phillips 1989). The time spent by stars in the post-AGB phase is a very strong function of their core mass (Renzini 1983). For high mass post-AGB stars, the evolution is very fast: a post-AGB star with core mass of $1.0M_\odot$ will have a nuclear burning time of only 25 yr (Tylenda 1989) and fades by a factor of 10 in luminosity on a similar timescale. These stars evolve too fast to make their planetary nebulae visible for long. Thus most planetary nebulae have central stars with core masses less than $0.64M_\odot$ (Tylenda & Stasińska 1989). On the other hand, very low mass post-AGB stars ($M < 0.55M_\odot$) evolve so slowly that before they raise their temperature to $3 \times 10^4\text{K}$ (needed to ionize hydrogen) the material expelled in the AGB phase has completely dissipated into the interstellar medium. These stars, termed ‘lazy post-AGB’ (Renzini 1981), will not appear as planetary nebulae. Therefore, considering the lifetime of post-AGB stars and the dynamical ages of the planetary nebulae, the central stars of planetary nebulae have to be post-AGB stars with core mass in a narrow range of $0.55\text{--}0.64M_\odot$ (Tylenda & Stasińska 1989, also see Buzzoni et al. 2006 Fig. 15 for a nice illustration of the mass dependent PN visibility). This core mass range corresponds roughly to an initial mass of $1\text{--}3M_\odot$ (Weidemann 2000). Lazy post-AGB stars and those post-AGB stars that live longer than 30000 years will form a diffuse ionizing field capable of ionizing the

neutral gas in the larger scale interstellar medium.

However, our current understanding of the late stages of stellar evolution is fairly poor and we do not know the temperature and age distribution of these stars well. Most post-AGB stars observed are either hidden inside planetary nebulae or observed when they are not yet hot enough to ionize the nebula. Few hot naked post-AGB stars have been observationally identified (Napiwotzki 1998; Brown et al. 2000; Weston et al. 2010), which may be due to strong observational bias since they will be very luminous in the extreme UV but very faint in the optical. Therefore, it is uncertain what fraction of post-AGB stars contribute to the large-scale photo-ionizing field and what fraction are hidden inside planetary nebulae.

Fortunately, there are two clues indicating that planetary nebulae do not dominate the line luminosity in most of our line-emitting galaxies. First, if the line emission is dominated by planetary nebulae, their kinematics should follow the stellar kinematics exactly. However, Sarzi et al. (2006) showed that the ionized-gas kinematics is decoupled from the stellar kinematics in the majority of galaxies in their sample.

Second, we can estimate the total [O III] luminosity contributed by planetary nebulae by integrating the planetary nebula luminosity function. We take the double exponential function given by Ciardullo et al. (1989),

$$\log N(M) = 0.133M + \log[1 - e^{3(M^* - M)}] + \text{const}, \quad (11)$$

where M is defined as $M_{[\text{O III}]} = -2.5 \log F_{[\text{O III}]} - 13.74$. The bright cut-off magnitude M^* is -4.47 . The faint cut-off magnitude is 8 mags fainter than M^* (Henize & Westerlund 1963). The normalization is usually given as the total number of planetary nebulae within the two cut-off magnitudes divided by the total luminosity of the galaxy. We adopt the median value reported by Buzzoni et al. (2006) for a sample of early-type galaxies, which is $N = 1.65 \times 10^{-7} L_{\text{gal}}/L_\odot$. With these, we found the total [O III] luminosity produced by planetary nebulae should be $L([\text{O III}]) = 1.35 \times 10^{28} L_{\text{gal}}/L_\odot \text{ erg s}^{-1}$. To estimate the total PN light we observed through the fiber, we should use the fiber magnitude to derive L_{gal} . For the 25% passive red galaxies at $0.09 < z < 0.1$ with the brightest total line luminosity, the median V-band absolute magnitude within the fiber aperture (derived using the fiber mags) is -20.09 . This produces a median [O III] luminosity of $1.21 \times 10^{38} \text{ erg s}^{-1}$, much smaller than the median [O III] luminosity among these galaxies, which is $6.2 \times 10^{39} \text{ erg s}^{-1}$. Therefore, we conclude that planetary nebulae is a minor contributor to the total line emission in these galaxies.

Can the diffuse ionizing field produced by naked post-AGB stars explain what we see? In this case, the sources are distributed like the stars and will produce the observed ionization parameter gradient and its luminosity dependence. The question is whether there are enough ionizing photons and what ionization parameter they can produce.

Binette et al. (1994) argue that the diffuse ionizing field has many more ionizing photons than planetary nebulae can produce, especially when the stellar population gets older than 3 Gyr. They estimate a total $Q_0 \sim 1 \times 10^{41} \text{ s}^{-1} M_\odot^{-1}$. The median stellar mass

with the fiber aperture for the 25% passive galaxies at $0.09 < z < 0.1$ with the brightest total line luminosity is $2.1 \times 10^{10} M_\odot$. Assuming all post-AGB ionizing photons are completely absorbed and on average it takes 2.2 photoionizing photons to produce one $H\alpha$ photon, this will produce a median $H\alpha$ luminosity of $2.9 \times 10^{39} \text{ergs}^{-1}$, which is about 1/3 of the median observed $H\alpha$ luminosity $8.3 \times 10^{39} \text{ergs}^{-1}$ (before extinction correction, but we expect the extinction to be small). Considering the uncertainties on Q_0 and other parameters involved in the calculation, this can be considered as a good agreement. This luminosity is much larger than the contribution from all planetary nebulae. More detailed calculations by Stasińska et al. (2008) and Cid Fernandes et al. (2011) yield similar results. Thus, post-AGB stars can produce enough ionizing photons to account for most of the line luminosity, as long as all these photons are trapped inside the galaxy. This latter question is related with how the gas clouds are distributed relative to the post-AGB stars.

In light of the decoupling of the gas kinematics from the stellar kinematics, let us assume that the line-emitting gas clouds are randomly distributed in relation to the post-AGB stars. In this case, we can estimate the ionization parameter by multiplying the Q_0 for post-AGB into Fig. 19. This yields an ionization parameter of $\log U = -5.2$ at 1 kpc, a factor of 10 lower than what is required ($\log U \sim -3.5$ from Figure 17, or -4 according to Binette et al. 1994). Therefore, although there may be enough photons from post-AGB stars to produce the total line luminosity, in our model the light is deposited onto clouds far away from the ionizing sources. In consequence, the flux is significantly reduced and the resulting ionization structure and line ratios are very different from the expectation from clouds closer to the ionizing sources.

A possible solution might be that clouds closest to individual post-AGB stars dominate in luminosity; if this were so, because they also have the highest ionization parameters, the luminosity-weighted average ionization parameter among all clouds would be raised. Here we determine that this solution is unlikely to work. To evaluate this possibility, we compute the average spacing between post-AGB stars using a rough number density computed by dividing the total ionizing flux by that from an average star. We use an individual post-AGB luminosity of $10^4 L_\odot$, significantly higher than average, which maximizes the contribution of individual stars in this calculation. With this luminosity, the inter-spacing is around 85 pc at $r = 1$ kpc and increases outwards. For gas clouds that are randomly distributed with regard to the post-AGB stars, the luminosity each cloud receives is $\text{Flux} \times \text{Area}$. The Flux consists of two components, the diffuse background F_b , and the flux from its nearest post-AGB star $Q_1/(4\pi r^2)$. Over a spherical volume with diameter equal to the inter-post-AGB spacing (r_{\max}), the total luminosity due to the diffuse background is

$$L_{bkgd} = F_b \frac{4\pi}{3} r_{\max}^3 n_c \langle A \rangle, \quad (12)$$

where n_c is the number density of gas clouds and $\langle A \rangle$ is the average projected cloud area. The total luminosity

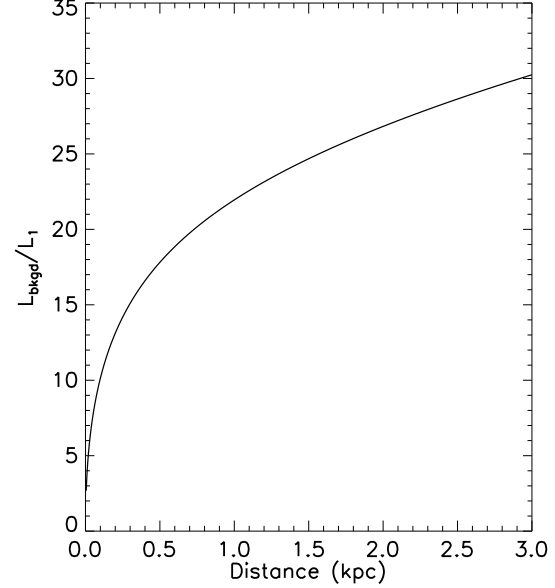


FIG. 24.— The ratio between emission line luminosity produced by diffuse pAGB ionizing background shining on randomly distributed clouds and that produced by a single nearby pAGB star as a function of radius. This indicates that the diffuse background is dominant in ionizing randomly distributed clouds, confirming the predicted ionization parameter.

due to an individual post-AGB star is

$$L_1 = \left(\int_0^{r_{\max}} \frac{Q_1}{4\pi r^2} 4\pi r^2 dr \right) n_c \langle A \rangle \quad (13)$$

$$= Q_1 r_{\max} n_c \langle A \rangle \quad (14)$$

where Q_1 is the total photoionizing photon output rate of the star.

Figure 24 shows the ratio L_{bkgd}/L_1 as a function of radius for the $\gamma = 1.5$ model. Except for the very central part of the galaxy, the luminosity due to the background is significantly larger than that due to individual nearby post-AGB stars. This result suggests the ionizing field produced by post-AGB stars is fairly smooth in most parts of the galaxies. The luminosity-weighted ionization parameter should be fairly close to what we showed in Fig. 19. Granularity in the ionization field is thus unlikely to cause a substantially increased ionization parameter.

Increasing the ionization parameter requires the clouds to be closer to the post-AGB stars. A factor of 4 decrease in average distance would probably be enough to bring the ionization parameter into the right ballpark. To achieve this, either the clouds must originate from progenitors of the post-AGB stars or the post-AGB stars must be preferentially distributed near the warm/cool gas. Since the gas is quite often kinematically decoupled from the stars, both scenarios require that the post-AGBs share the same origin as the gas, rather than that of the main stellar population. Among all post-AGB stars, those with the largest core mass dominate in luminosity, which are also the youngest. If both the gas and the dominant post-AGB stars are associated with the most recent star formation episode, the dominant

post-AGB population might share a similar spatial distribution and kinematics with the gas. This scenario would help resolve the deficit in ionization parameter. However, because our sample selection involves a cut in $D_n(4000)$ which would exclude systems with more than a few percent⁵ of their stellar mass from a young stellar population ($< 1\text{Gyr}$), we consider this scenario unlikely. Nonetheless, it can be tested by looking at planetary nebulae kinematics to see whether they follow the stars or the gas.

Another possible scenario is that the cool gas responsible for the emission indeed originates from the progenitors of the post-AGB stars. They have expanded so much that they no longer appear as planetary nebulae, but still are not as far as a randomly positioned cloud. At this point, they are completely dispersed in the interstellar medium and are carried away by the motion of the hot gas and thus they appear kinematically decoupled from the stars. In this picture, the cold gas has an internal origin, but their kinematics is driven by the hot gas, which is kinematically decoupled from the stars, perhaps due to mergers and the collisional nature of the gas.

Another possible solution is that the stars have a distribution that is better resembled by a thick disk than a sphere. Compared to the spherical symmetric distribution we assumed, a flatter disk distribution would bring the stars closer to the gas, raising the ionization parameter. We can investigate this by looking at whether the stronger line emitting systems are preferentially more disk-like in morphology. We leave this for future investigation.

A final possible solution is that abundance of post-AGB stars is much larger than predicted.

To summarize, the post-AGB star photoionization model can naturally produce the general variation of ionization parameter with radius, including the sharp rise at small radius and gentle decline on large radius. It is also able to produce the overall direction of the luminosity-dependence of the line ratio gradient. This result strongly indicates that the spatial distribution of the true ionizing source is similar to the stellar distribution. However, based on our current knowledge about post-AGB stars, the ionization parameter they produce would be too small, even though they may have sufficient total luminosity. The uncertainty in the number density of post-AGB stars is still too large (Brown et al. 2000, 2008; Weston et al. 2010) and observations are too scarce. Deeper observations and larger surveys of them are necessary to settle these questions.

6.3.4. Other possible distributed photoionizing sources

Low-mass X-ray binaries and extreme horizontal branch stars are two other evolved populations that could provide some additional ionizing photons. However, Sarzi et al. (2010) have argued that they would produce much fewer photoionizing photons than post-AGB stars. Thus they are unlikely to be responsible on their

own for the observed line emission, or to make up the ionization parameter deficit found above.

Recently, high-mass X-ray binaries (HMXBs) and ultraluminous X-ray sources (ULXs) (ULXs) have also been invoked to explain the LINER-like emission (McKernan et al. 2011). However, we do not think this population would solve the deficit either. First, in an old galaxy like those in our sample, there would be very few high-mass X-ray binaries, because they are only associated with young stellar populations. Second, both HMXBs and ULXs are X-ray bright so they should have been included in the accounting by Eracleous et al. (2010), who showed that extrapolating the X-ray luminosity in the nuclear region of LINERs to the ultraviolet does not yield enough ionizing photons to produce the nuclear $\text{H}\alpha$ luminosity observed. Therefore, these components would make at most a minor contribution.

The hot X-ray emitting gas is also a distributed ionizing source that can produce LINER-like emission (Voit & Donahue 1990; Donahue & Voit 1991). Because the hot gas density approximately follows the square root of the stellar density, the X-ray emission should have the same luminosity density profile as the stars. Therefore, it can also produce the expected trend in line ratio gradient and luminosity dependence.

However, the X-ray gas is unlikely to produce enough ionizing photons. For the typical galaxy in our sample (the 25% passive red galaxy at $0.09 < z < 0.1$ with the brightest total line luminosity), with a median stellar mass of $7.5 \times 10^{10} M_\odot$ and $L_B = 2.8 \times 10^{10} L_\odot$, the X-ray luminosity from the hot gas is on the order of $10^{41} \text{erg s}^{-1}$ (O’Sullivan et al. 2001), much lower than the total ionizing luminosity of post-AGB stars ($\sim 10^{42} \text{erg s}^{-1}$). Therefore, they should be subdominant to post-AGB stars and would have an even lower contribution to the ionization parameter.

6.4. Fast radiative shocks

Shocks are prevalent in many astrophysical phenomena, such as supernova explosions, stellar winds, AGN jets and outflows, cloud collisions, etc. Collisional excitation in the post-shock medium can produce line ratios similar to LINERs. The fast radiative shock could also photoionize the precursor, unshocked regions. When combined with the emission lines produced in the cooling zone of the shock, the resulting line ratios are similar to those of Seyferts (Groves et al. 2004b). In the section, we investigate whether the shock model can reproduce the trends we observed in the data.

Because the shock-only model produces a better match to the LINER-like line ratios observed in these passive red galaxies, we only consider this model. In this model, the line ratios are determined by four parameters: shock velocity, magnetic field strength, density, and metallicity. Because the strong dependence of line ratios on shock velocity, if there are a wide range of shock velocities present in a galaxy, we should observe different widths for different lines in the shock-only model. The data do show different widths for different emission lines. The issue is whether the velocity dependence of line ratios can produce the observed width difference in the right direction.

In Section 5, we showed that the $[\text{O III}]$ line is on average wider than $[\text{S II}]$ lines by 16%. This means that those high-velocity line-emitting regions have a higher

⁵ The exact mass fraction of the young population tolerable by our $D_n(4000)$ cut depends on the assumptions used in the stellar population modeling. Assuming an old simple stellar population with solar metallicity and an age of 4.6 Gyr, which yields the observed median $D_n(4000)$ of 1.9, our $D_n(4000)$ cut at $z \sim 0.1$ can only tolerate at most 2% of its stellar mass coming from a population younger than 1 Gyr.

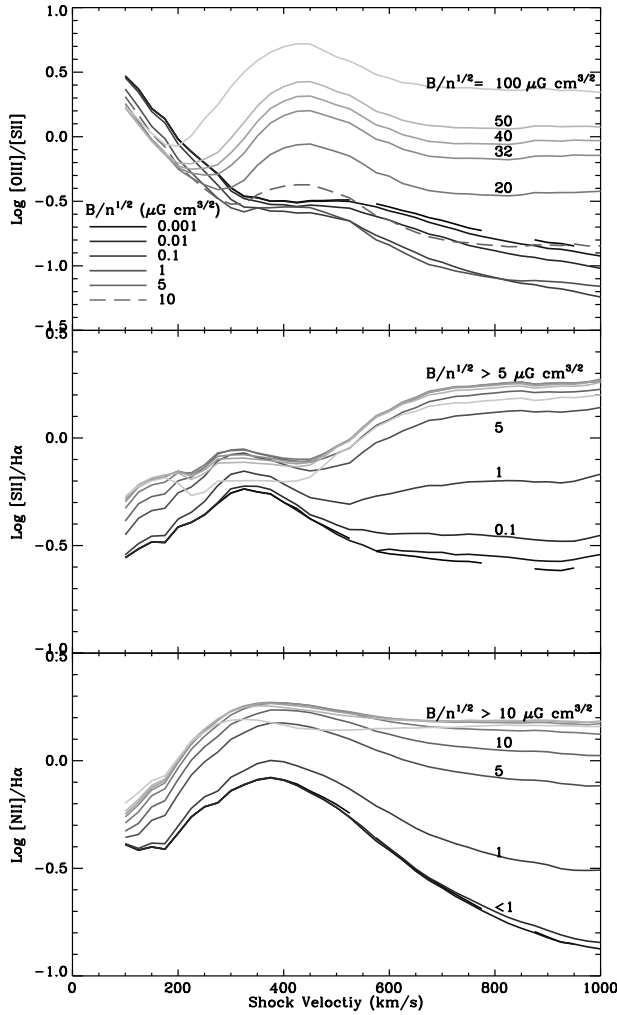


FIG. 25.— Line ratios produced by shocks as a function of shock velocity for different magnetic field strengths. The curves are plotted from dark black to light grey in order of increasing magnetic field strength.

$[\text{O III}]/[\text{S II}]$ ratios than low-velocity regions. Although the bulk-motion velocity of clouds is not the same as the shock velocity, we expect in general faster moving clouds in a galaxy would generate faster shocks when they collide. If the lines are mostly produced in post-shock cooling zones resulting from cloud collisions, to explain the data would require higher $[\text{O III}]/[\text{S II}]$ ratio to be produced in faster shocks.

We look at the line ratio dependence on velocity in the fast shock models given by Allen et al. (2008), which are run using the MAPPINGS III code. Figure 25 shows the $[\text{O III}]/[\text{S II}]$ ratio as a function of shock velocity for different magnetic field strengths. This model is run with solar metallicity and a pre-shock gas density of $n = 100 \text{ cm}^{-3}$. In most part of the parameter space, $[\text{O III}]/[\text{S II}]$ decreases with increasing velocity. Only for $B/n^{1/2} \geq 10 \mu\text{G cm}^{3/2}$ and for shock velocity between 250 and 400 km/s, does the $[\text{O III}]/[\text{S II}]$ ratio increase with velocity. However, these parameter ranges do not

produce the right velocity dependence for the other line ratios. The $[\text{S II}]$ lines in our sample is narrower than $\text{H}\alpha$ lines by 7% on average, and the $[\text{N II}]$ lines are having roughly the same width as $\text{H}\alpha$ lines. This requires the $[\text{S II}]/\text{H}\alpha$ to decrease with velocity and $[\text{N II}]/\text{H}\alpha$ to stay constant with velocity. However, the model predicts a strongly increasing $[\text{N II}]/\text{H}\alpha$ and a slightly increasing/flat $[\text{S II}]/\text{H}\alpha$ with velocity in those particular parameter ranges, inconsistent with the requirement to explain the observations. Therefore, although shocks certainly exist in most galaxies, they are probably not the dominant source in producing the extended line emission in these passive red galaxies.

Our conclusion agrees with the conclusion of Sarzi et al. (2010), who also argued against the shock scenario as the dominant ionizing source based on the low circular velocity and low velocity dispersion observed, lack of morphological correlation between line emission structure and line ratio structure, and the flat EW distribution.

On the other hand, Annibali et al. (2010) argued that shocks could be important in the central regions of some early-type galaxies as the AGN jet-driven outflows or accretion onto a massive black hole could possibly reach the high velocities (300-500 km/s) required by the shock models. Shocks certainly exist in these situations, but having the right condition for shocks to occur does not mean shocks are directly responsible for the ionization of the gas. Further proof, such as a correlation between line ratio and velocity, is necessary.

In a totally different case, in ultraluminous infrared galaxies (ULIRGs), shocks could indeed be responsible for producing the strong LINER-like emission found there (Monreal-Ibero et al. 2006, 2010; Alonso-Herrero et al. 2010). As these galaxies are usually results of major mergers, stronger and faster shocks are more prevalent. Star formation in these galaxies might also be partially responsible for the line emission.

7. CONCLUSIONS

In this paper, we studied the spatial distribution of LINER-like line emission in passive red galaxies by comparing the nuclear emission luminosity measured from the Palomar survey with the larger aperture data from SDSS. We find strong evidence for line ratio gradients. We also find that different emission lines have different velocity widths, in contrast to the uniform velocity widths in star-forming galaxies. We have reached the following conclusions.

1. In the majority of line-emitting red galaxies, the line emission is spatially extended and its intensity peaks at the center. The average $\text{H}\alpha$ surface brightness profile can be well approximated by a power-law with an index of -1.28 . Line-emitting red galaxies identified with nuclear aperture spectroscopy or those with extended aperture spectroscopy are essentially the same population.
2. Line ratio gradients exist in these line-emitting red galaxies, with the very center having generally larger $[\text{N II}]/\text{H}\alpha$, $[\text{S II}]/\text{H}\alpha$, and smaller $[\text{O III}]/[\text{S II}]$ than the outskirts. The $[\text{O III}]/[\text{S II}]$ gradient requires an increasing ionization parameter towards larger distances. Because the cool gas

density is likely to fall with radius at a much slower rate than r^{-2} , an outward increasing ionization parameter strongly disfavors AGN as the dominant ionizing mechanism in these galaxies.

3. The line ratio gradient can be produced by ionizing sources that are distributed like the stars. This model also predicts different line ratio gradient trends in bright and faint galaxies, which are generally matched by observations.
4. The leading candidate for the ionizing source is the population of post-AGB stars. The majority of these stars cannot be central stars of planetary nebulae, but have to be naked post-AGB stars creating a diffuse ionizing field. However, the ionization parameter produced by post-AGB stars falls short of the required value by more than a factor of 10. Either the abundance of post-AGB stars is underpredicted or their spatial distribution has to be much closer to the gas clouds than assumed. The latter possibility would suggest a common origin of the gas and the post-AGB stars.
5. Different emission lines in passive red galaxies often have different widths. The [O III] is on average wider than [S II] by 16%; [N II] and H α are wider than [S II] by $\sim 8\%$. The width ratios do not vary as a function of aperture size. This latter result strongly suggests that the width ratio is not produced by the combination of the line ratio gradient and rotation, but more likely due to a multiphase ISM in these galaxies.
6. We considered shock models for producing these trends. Because line ratios produced in the cooling zone of the shocks have a strong dependence on the shock velocity, these models naturally produce width differences among different lines. However, their velocity dependence generate opposite width differences from what we observe. Therefore, shocks are strongly disfavored by our results as the dominant ionizing source in these passive red galaxies. However, it may be responsible for producing LINER-like emission found in ULIRGs.
7. The systematically different [N II]/H α ratio profiles between bright and faint galaxies (Fig. 23) suggest that the gas-phase metallicity is dependent on galaxy luminosity.

Our result strongly disfavors AGN as the dominant ionization mechanism for the line emission in passive red galaxies. However, it does not mean that all LINERs have nothing to do with AGN. For a large fraction of those nuclear LINERs identified in the Palomar survey, accretion activity probably does exist, as evidenced by the detection of compact radio core (Nagar et al. 2000) and X-ray point sources in their centers (Ho et al. 2001). Our result does mean that the optical line emission in most of them are probably powered by sources unrelated with AGN activity. The AGN is probably significantly less luminous in line emission than previously thought and dominates on much smaller scales than 100 pc. This result also helps to resolve the energy budget problem

reported for most of these “nuclear LINERs.” The large X-ray and radio detection fraction may be a result of more fuel supply in these relatively “gas-rich” early-type galaxies.

For line emission found in apertures covering much larger area, such as in the SDSS at $z > 0.02$, the line emission is nearly always dominated by extended emission unrelated with AGN activity. Therefore, most studies using line emission to derive AGN bolometric luminosity for LINER-like objects using SDSS data (e.g. Kauffmann et al. 2003; Kewley et al. 2006; Kauffmann & Heckman 2009; Choi et al. 2009) or higher- z surveys (Bongiorno et al. 2010) probably need to have their results re-inspected. The impact is probably most significant for objects with $L_{[\text{OIII}]} \lesssim 10^6 L_{\odot}$, for which we have demonstrated that the ionizing sources are outside the nucleus. The exact threshold is also a function of the aperture size and galaxy luminosity.

Although we only focused on passive red galaxies in our investigation, the result should also apply to LINER-like objects among younger red-sequence galaxies. Those red LINER-like objects with smaller $D_n(4000)$ probably also have some weak star-forming activity contributing to their line emission, as demonstrated in Fig. 4.

The extended line emission is present in more than half of red-sequence galaxies and is much more luminous than most low-ionization AGNs. Based on the Palomar results, only the brightest few percent of low-ionization AGNs have a chance of detection in large aperture spectroscopy data.

Our result favors a distribution of ionizing sources that follows the stars, but does not confirm post-AGB stars as the ionizing sources. Post-AGB stars are the only source that has sufficient total energy to produce the observed emission lines. However, they fall short in the ionization parameter. This mystery awaits future observations to resolve.

If the post-AGB stars are confirmed as the ionization sources, the LINERs can provide a window onto the gas dynamics of passive red galaxies. The total flux from post-AGB stars stay fairly constant with the age of the stellar population, except for the first Gyr after the starburst. In this case, our results would then indicate that differing amounts of line emission in these galaxies is mainly an indicator of different amounts of cool/warm gas. We could therefore use the line strength observed to study the cooling and heating of warm gas in early-type galaxies.

This study shows the huge amount of information we can learn from wide wavelength range, well-calibrated, high-resolution spectroscopy. It also demonstrates the power of large statistical samples. More detailed, spatially resolved IFU studies of nearby early-type galaxies are obviously the next step to confirm our results. An important lesson from this work is that the inclusion of [N II], H α , and [S II] in the resolved spectra was essential to constraining the ionizing sources; indeed, in our case the broad wavelength range is arguably more important than the spatial resolution available to IFU observations. This result motivates the use of IFU techniques with broad wavelength coverage to maximize the available information.

We would like to thank the referee for detailed and thorough comments, which helped us improve the paper. RY would like to thank Guangtun Zhu and Timothy Heckman for illuminating discussions that greatly improved this work. RY and MB acknowledge the support of the NSF Grant AST-0908354, NASA Grant 08-ADP08-0019m, NASA Grant 08-ADP08-0072, and a Google Research Award.

Funding for the Sloan Digital Sky Survey (SDSS) has been provided by the Alfred P. Sloan Foundation, the Participating Institutions, the National Aeronautics and Space Administration, the National Science Foundation, the U.S. Department of Energy, the Japanese Monbuka-

gakucho, the Max Planck Society, and the Higher Education Funding Council for England. The SDSS Web site is <http://www.sdss.org/>. The SDSS is managed by the Astrophysical Research Consortium (ARC) for the Participating Institutions. The Participating Institutions are The University of Chicago, Fermilab, the Institute for Advanced Study, the Japan Participation Group, The Johns Hopkins University, Los Alamos National Laboratory, the Max-Planck-Institute for Astronomy (MPIA), the Max-Planck-Institute for Astrophysics (MPA), New Mexico State University, the University of Pittsburgh, Princeton University, the United States Naval Observatory, and the University of Washington.

REFERENCES

- Abazajian, K. N., et al. 2009, *ApJS*, 182, 543
- Allen, M. G., Groves, B. A., Dopita, M. A., Sutherland, R. S., & Kewley, L. J. 2008, *ApJS*, 178, 20
- Allen, S. W., Dunn, R. J. H., Fabian, A. C., Taylor, G. B., & Reynolds, C. S. 2006, *MNRAS*, 372, 21
- Alonso-Herrero, A., García-Marín, M., Rodríguez Zaurín, J., Monreal-Ibero, A., Colina, L., & Arribas, S. 2010, *A&A*, 522, A7
- Annibali, F., Bressan, A., Rampazzo, R., Zeilinger, W. W., Vega, O., & Panuzzo, P. 2010, *A&A*, 519, A40+
- Bacon, R., et al. 2001, *MNRAS*, 326, 23
- Balogh, M. L., Morris, S. L., Yee, H. K. C., Carlberg, R. G., & Ellingson, E. 1999, *ApJ*, 527, 54
- Beers, T. C., Flynn, K., & Gebhardt, K. 1990, *AJ*, 100, 32
- Bernardi, M., Shankar, F., Hyde, J. B., Mei, S., Marulli, F., & Sheth, R. K. 2010, *MNRAS*, 404, 2087
- Binette, L., Magris, C. G., Stasinska, G., & Bruzual, A. G. 1994, *A&A*, 292, 13
- Blanton, M. R., Kazin, E., Muna, D., Weaver, B. A., & Price-Whelan, A. 2011, *AJ*, 142, 31
- Blanton, M. R., & Roweis, S. 2007, *AJ*, 133, 734
- Blanton, M. R., et al. 2005, *AJ*, 129, 2562
- Bongiorno, A., et al. 2010, *A&A*, 510, A56+
- Brown, T. M., Bowers, C. W., Kimble, R. A., Sweigart, A. V., & Ferguson, H. C. 2000, *ApJ*, 532, 308
- Brown, T. M., Smith, E., Ferguson, H. C., Sweigart, A. V., Kimble, R. A., & Bowers, C. W. 2008, *ApJ*, 682, 319
- Bruzual, G., & Charlot, S. 2003, *MNRAS*, 344, 1000
- Buson, L. M., et al. 1993, *A&A*, 280, 409
- Buzzoni, A., Arnaboldi, M., & Corradi, R. L. M. 2006, *MNRAS*, 368, 877
- Caon, N., Macchetto, D., & Pastoriza, M. 2000, *ApJS*, 127, 39
- Capetti, A., & Baldi, R. D. 2011, *A&A*, 529, A126+
- Cappellari, M., et al. 2011, *MNRAS*, 413, 813
- Choi, Y.-Y., Woo, J.-H., & Park, C. 2009, *ApJ*, 699, 1679
- Ciardullo, R., Jacoby, G. H., Ford, H. C., & Neill, J. D. 1989, *ApJ*, 339, 53
- Cid Fernandes, R., Stasińska, G., Mateus, A., & Vale Asari, N. 2011, *MNRAS*, 249
- Constantin, A., & Vogeley, M. S. 2006, *ApJ*, 650, 727
- Davis, M., et al. 2003, in *Discoveries and Research Prospects from 6- to 10-Meter-Class Telescopes II*. Edited by Guhathakurta, Puragra. *Proceedings of the SPIE*, Volume 4834, pp. 161-172 (2003), ed. P. Guhathakurta, 161-172
- De Robertis, M. M., & Osterbrock, D. E. 1986, *ApJ*, 301, 727
- de Vaucouleurs, G., de Vaucouleurs, A., Corwin, Jr., H. G., Buta, R. J., Paturel, G., & Fouque, P. 1991, *Third Reference Catalogue of Bright Galaxies* (Springer)
- de Vaucouleurs, G., de Vaucouleurs, A., & Corwin, J. R. 1976, in *Second reference catalogue of bright galaxies*, 1976, Austin: University of Texas Press., 0+
- Dehnen, W. 1993, *MNRAS*, 265, 250
- di Serego Alighieri, S., Trinchieri, G., & Brocato, E. 1990, in *ASSL Vol. 160: Windows on Galaxies*, 301+
- Donahue, M., & Voit, G. M. 1991, *ApJ*, 381, 361
- Donahue, M., & Voit, G. M. 1997, in *Astronomical Society of the Pacific Conference Series*, Vol. 115, *Galactic Cluster Cooling Flows*, ed. N. Soker, 48
- Dopita, M. A., Groves, B. A., Sutherland, R. S., Binette, L., & Cecil, G. 2002, *ApJ*, 572, 753
- Dopita, M. A., & Sutherland, R. S. 1995, *ApJ*, 455, 468
- , 1996, *ApJS*, 102, 161
- Eisenstein, D. J., et al. 2011, *AJ*, 142, 72
- Eracleous, M., Hwang, J. A., & Flohic, H. M. L. G. 2010, *ApJ*, 711, 796
- Faber, S. M., et al. 1997, *AJ*, 114, 1771
- Ferland, G. J., & Netzer, H. 1983, *ApJ*, 264, 105
- Ferrarese, L., et al. 2006, *ApJS*, 164, 334
- Filippenko, A. V. 1985, *ApJ*, 289, 475
- Filippenko, A. V., & Halpern, J. P. 1984, *ApJ*, 285, 458
- Glass, L., et al. 2011, *ApJ*, 726, 31
- Goudfroi, P., Hansen, L., Jorgensen, H. E., & Norgaard-Nielsen, H. U. 1994, *A&AS*, 105, 341
- Groves, B. A., Dopita, M. A., & Sutherland, R. S. 2004a, *ApJS*, 153, 9
- , 2004b, *ApJS*, 153, 75
- Halpern, J. P., & Steiner, J. E. 1983, *ApJ*, 269, L37
- Heckman, T. M. 1980, *A&A*, 87, 152
- Heckman, T. M., Baum, S. A., van Breugel, W. J. M., & McCarthy, P. 1989, *ApJ*, 338, 48
- Henize, K. G., & Westerlund, B. E. 1963, *ApJ*, 137, 747
- Hernquist, L. 1990, *ApJ*, 356, 359
- Ho, L. C. 2008, *ARA&A*, 46, 475
- Ho, L. C., Filippenko, A. V., & Sargent, W. L. 1995, *ApJS*, 98, 477
- Ho, L. C., Filippenko, A. V., & Sargent, W. L. W. 1996, *ApJ*, 462, 183
- , 1997a, *ApJS*, 112, 315
- , 1997b, *ApJ*, 487, 568
- Ho, L. C., et al. 2001, *ApJ*, 549, L51
- Jaffe, W. 1983, *MNRAS*, 202, 995
- Kauffmann, G., & Heckman, T. M. 2009, *MNRAS*, 397, 135
- Kauffmann, G., et al. 2003, *MNRAS*, 346, 1055
- Kaviraj, S. 2010, *MNRAS*, 406, 382
- Kewley, L. J., Dopita, M. A., Sutherland, R. S., Heisler, C. A., & Trevena, J. 2001, *ApJ*, 556, 121
- Kewley, L. J., Groves, B., Kauffmann, G., & Heckman, T. 2006, *MNRAS*, 372, 961
- Kim, D.-W. 1989, *ApJ*, 346, 653
- Kuntschner, H., et al. 2010, *MNRAS*, 408, 97
- Lauer, T. R., et al. 1995, *AJ*, 110, 2622
- , 2005, *AJ*, 129, 2138
- Lemaux, B. C., Lubin, L. M., Shapley, A., Kocevski, D., Gal, R. R., & Squires, G. K. 2010, *ApJ*, 716, 970
- Lilly, S. J., et al. 2007, *ApJS*, 172, 70
- Lubin, L. M., Gal, R. R., Lemaux, B. C., Kocevski, D. D., & Squires, G. K. 2009, *AJ*, 137, 4867
- Macchetto, F., Pastoriza, M., Caon, N., Sparks, W. B., Giallisco, M., Bender, R., & Capaccioli, M. 1996, *A&AS*, 120, 463
- Masegosa, J., Márquez, I., Ramírez, A., & González-Martín, O. 2011, *A&A*, 527, A23
- Masters, K. L., et al. 2010, *MNRAS*, 405, 783
- Mathews, W. G., & Brighenti, F. 2003, *ARA&A*, 41, 191
- McKernan, B., Ford, K. E. S., Yaqoob, T., & Winter, L. M. 2011, *MNRAS*, 413, L24
- Monreal-Ibero, A., Arribas, S., & Colina, L. 2006, *ApJ*, 637, 138
- Monreal-Ibero, A., Arribas, S., Colina, L., Rodríguez-Zaurín, J., Alonso-Herrero, A., & García-Marín, M. 2010, *A&A*, 517, A28
- Nagar, N. M., Falcke, H., Wilson, A. S., & Ho, L. C. 2000, *ApJ*, 542, 186
- Napiwotzki, R. 1998, in *Reviews in Modern Astronomy*, Vol. 11, *Reviews in Modern Astronomy*, ed. R. E. Schielicke, 3+
- O'Sullivan, E., Forbes, D. A., & Ponman, T. J. 2001, *MNRAS*, 328, 461
- Phillips, J. P. 1989, in *IAU Symposium*, Vol. 131, *Planetary Nebulae*, ed. S. Torres-Peimbert, 425-442
- Phillips, M. M., Jenkins, C. R., Dopita, M. A., Sadler, E. M., & Binette, L. 1986, *AJ*, 91, 1062
- Ravindranath, S., Ho, L. C., Peng, C. Y., Filippenko, A. V., & Sargent, W. L. W. 2001, *AJ*, 122, 653

- Renzini, A. 1981, in *Astrophysics and Space Science Library*, Vol. 88, *Physical Processes in Red Giants*, ed. I. Iben Jr. & A. Renzini, 431–446
- Renzini, A. 1983, in *IAU Symposium*, Vol. 103, *Planetary Nebulae*, ed. D. R. Flower, 267–279
- Rest, A., van den Bosch, F. C., Jaffe, W., Tran, H., Tsvetanov, Z., Ford, H. C., Davies, J., & Schafer, J. 2001, *AJ*, 121, 2431
- Sandage, A., & Tammann, G. A. 1981, *A revised Shapley-Ames Catalog of bright galaxies*
- Sarzi, M., et al. 2006, *MNRAS*, 366, 1151
- . 2010, *MNRAS*, 402, 2187
- Schawinski, K., Thomas, D., Sarzi, M., Maraston, C., Kaviraj, S., Joo, S., Yi, S. K., & Silk, J. 2007, *MNRAS*, 382, 1415
- Schawinski, K., et al. 2010, *ApJ*, 711, 284
- Schoenberger, D. 1983, *ApJ*, 272, 708
- Shields, J. C., et al. 2007, *ApJ*, 654, 125
- Sparks, W. B., Macchetto, F., & Golombek, D. 1989, *ApJ*, 345, 153
- Stasińska, G., Vale Asari, N., Cid Fernandes, R., Gomes, J. M., Schlickmann, M., Mateus, A., Schoenell, W., & Sodré, Jr., L. 2008, *MNRAS*, 391, L29
- Stoughton, C., et al. 2002, *AJ*, 123, 485
- Tylenda, R. 1989, in *IAU Symposium*, Vol. 131, *Planetary Nebulae*, ed. S. Torres-Peimbert, 531–537
- Tylenda, R., & Stasińska, G. 1989, *A&A*, 217, 209
- Voit, G. M., & Donahue, M. 1990, *ApJ*, 360, L15
- Walsh, J. L., Barth, A. J., Ho, L. C., Filippenko, A. V., Rix, H.-W., Shields, J. C., Sarzi, M., & Sargent, W. L. W. 2008, *AJ*, 136, 1677
- Wang, J., Heckman, T. M., & Lehnert, M. D. 1997, *ApJ*, 491, 114
- Weidemann, V. 2000, *A&A*, 363, 647
- Weston, S., Napiwotzki, R., & Catalán, S. 2010, in *American Institute of Physics Conference Series*, Vol. 1273, *American Institute of Physics Conference Series*, ed. K. Werner & T. Rauch, 197–202
- Yan, R. 2011, *AJ*, 142, 153
- Yan, R., Newman, J. A., Faber, S. M., Konidaris, N., Koo, D., & Davis, M. 2006, *ApJ*, 648, 281
- Yan, R., et al. 2011, *ApJ*, 728, 38
- York, D. G., et al. 2000, *AJ*, 120, 1579
- Zeilinger, W. W., et al. 1996, *A&AS*, 120, 257